https://doi.org/10.5194/gmd-2024-175
Preprint. Discussion started: 17 January 2025

Geoscientific Model Development
Discussions

The glacial systems model (GSM) Version 24G

Lev Tarasov[1], Benoit S. Lecavalier[1,2], Kevin Hank[3], and David Pollard[4]

[1]Department of Physics and Physical Oceanography, Memorial University of Newfoundland and Labrador, St. John's, Canada, A1B 3X7
[2]Defence Research & Development Canada (DRDC), Suffield Research Centre, PO Box 4000, Station Main, Medicine Hat, T1A 8K6, Alberta, Canada
[3]Natural Environment Research Council, British Antarctic Survey, High Cross, Madingley Road, Cambridge, CB3 0ET, United Kingdom
[4]Earth and Environmental Systems Institute, Pennsylvania State University, University Park, PA 16802, USA; and Department of Earth, Geographic, and Climate Sciences, University of Massachusetts, Amherst, MA 01003, USA

Correspondence: Lev Tarasov (lev@mun.ca)

Abstract. We document the glacial system model (GSM), which includes a 3D thermo-mechanically coupled glaciological ice sheet model. The GSM is designed for large ensemble modelling in glacial cycle contexts. A distinguishing feature is the extent to which it addresses relevant uncertainties. The GSM has evolved from 2 and a half decades of effort to constrain last glacial cycle evolution of each major ice sheet. The core ice dynamics uses a hybrid shallow-shelf and shallow-ice approximation. It also includes one of the largest range of relevant processes for this context of any model to date, ranging from visco-elastic glacial isostatic adjustment with 0-order geoidal deflection to state-of-the-art subglacial sediment production, transport, and deposition. Other relevant distinguishing features include: permafrost resolving bed-thermodynamics, a fast diagnostic solution of down-slope surface drainage and lake filling, subgrid hypsometric surface mass balance and ice flow, simple thermodynamic lake and sea ice representations, subglacial hydrology with dynamically evolving partitioning between distributed and channelized flow, and surface melt that physically accounts for insolation changes via a novel insolation above freezing scheme.

To address the most challenging part of paleo ice sheet modelling, the GSM includes both a 2D energy balance climate model and variants of traditional glacial indexed interpolation of fields from General Circulation Model (GCM) simulations, all under ensemble parametric specification. It also includes options for one and two way scripted coupling with climate models.

We demonstrate the significant errors that can ensue in the glacial cycle simulation of a single ice sheet when three aspects of glacial isostatic adjustment are ignored (as is typical). These are geoidal deformation, global ice load input, and correction of initial topography for present-day isostatic disequilibrium. We also draw attention to the relatively high sensitivity of the GSM (and presumably other ice sheet models) to the specification of the temperature dependence for basal sliding activation.

The associated code archive includes configuration options for all major last glacial cycle ice sheets as well as idealized geometries and validation test setups.

https://doi.org/10.5194/gmd-2024-175
Preprint. Discussion started: 17 January 2025

Geoscientific Model Development Discussions

1 Introduction

Paleo ice sheet modelling contexts have some features that impose distinct requirements in comparison to models designed for present-day and near future centennial scale modelling. For the latter, certain processes, such as subglacial sediment production, transport, and deposition, are effectively irrelevant (given their much longer characteristic time-scales, eg Drew and Tarasov, 2024), and others, such as glacial isostatic adjustment (GIA), can be more simply or more carefully approximated, depending on context and simulation time interval (Whitehouse et al., 2019). Furthermore, given the large uncertainties in climate forcing over a glacial cycle, ice sheet modelling for the purpose of constraining past ice sheet evolution requires large ensembles of simulations. This along with the O(100 kyr) glacial cycle timescale implies that computational costs are a much more critical consideration for paleo ice sheet modelling as compared to present-day modelling contexts.

The Glacial Systems Model (GSM) is a numerical model for simulating ice sheets and their interactions with the rest of the Earth system over glacial cycle time-scales. It features fully coupled components relevant to this context that, to date, are not found as a set in any other ice sheet model (some other current models used for paleo ice sheet modelling have many, but not all of the GSM features, *e.g.,* Winkelmann et al., 2011; Sato and Greve, 2012; Pollard et al., 2015; Quiquet et al., 2018; Robinson et al., 2020; Berends et al., 2022). For instance, the GSM is the only glaciological ice sheet model that can resolve englacial sediment transport nor subglacial sediment production due to quarrying (with otherwise only Pollard et al., 2015, having even a representation of subglacial sediment transport).

A key and distinguishing GSM design consideration is a focus on uncertainty quantification. This entails parametrization of as many significant glacial system uncertainties as is reasonably possible, given the much greater challenge in assessing structural modelling uncertainties. This results in the GSM currently having 30 (Patagonia) to 53 (North America) ensemble parameters for a single ice sheet. In contrast, all previous paleo ice sheet modelling studies not using the GSM (or its precursor, Tarasov and Peltier, 2004) use fewer than 7 parameters (*e.g.,* Albrecht et al., 2020, use 4 ensemble parameters for ensemble modelling of the last glacial cycle Antarctic ice sheet). The GSM (uniquely to date) also has noise insertion options for partial quantification of structural uncertainties (*i.e.* model uncertainties not captured by ensemble parameters).

Given the large ensemble requirement for paleo ice sheet modelling, the GSM is highly optimized for serial computation, with *e.g.,* 205 kyr of Antarctic simulation at 40 km resolution taking about 10 hours on a (circa 2016) single Intel Xeon E5-2650 (2.3GHz) core. The lack of parallelization limits spatial grid resolution to about 10 km for continental scales, with 0.5^o by 0.25^o longitude by latitude being the current default. However, to partially compensate for limited spatial resolution, the GSM includes a state-of-the-art subgrid hypsometric surface mass-balance and ice flow model (Le Morzadec et al., 2015).

Another important feature is that the model has been configured for all last glacial cycle ice sheets (including Antarctic, Greenland, North American, Eurasian, Icelandic, Patagonian, and Tibetan), and includes options for one and two way coupling with external climate models. The GSM's internal climate representation enables full Pleistocene simulations of Northern Hemispheric ice sheets in approximate accord with inferences for past sea level from benthic δ^{18}O records with simulations only driven by orbital and greenhouse gas forcing (Drew and Tarasov, 2024).

https://doi.org/10.5194/gmd-2024-175
Preprint. Discussion started: 17 January 2025

Geoscientific Model Development
Discussions
Open Access

Table 1. GSM components and relevant section for description.

Component/process	subsection
hybrid ice dynamics	2.4 and A1
basal drag	2.5
ice and bed thermodynamics	2.6
surface melt and refreezing	2.7.1
submarine melt	2.7.2
ice shelf calving	2.7.3
tidewater calving	2.7.4
lacustrine calving	2.7.5
surface drainage and lake formation	2.8
lake and sea ice formation	2.9
glacial indices	2.10.1
atmospheric climate forcing	2.10.2
orographic precipitation downscaling	2.10.3
ocean climate forcing	2.10.4
subgrid mass balance and ice flow	2.11
mass balance nudging	2.12
subglacial hydrology	2.13
subglacial sediment processes	2.14
GIA solver	2.15
noise injection	2.16

Though the model continues to evolve, it is now at a stage and in a form appropriate for initial public release. Below we document the GSM and provide example test results of the impact of some of its relatively unique features.

2 Model description

The GSM includes a number of distinct, fully coupled components (cf Table 1). The hybrid shallow-shelf/shallow-ice (SSA/SIA) dynamical core is a modified version of the PSU3D ice sheet model (Pollard and DeConto, 2012; Pollard et al., 2015; Pollard and DeConto, 2020). This dynamical core includes an appropriate grounding line flux parameterization (Schoof, 2007; Pollard and DeConto, 2020) and is able to capture marine ice shelf instabilities (Pollard et al., 2015). The main differences from that of Pollard et al. (2015) are conversion to Fortran 90 standards, the addition of the NSPCG generalized numerical solver (Kincaid et al., 1989) for solving the SSA stress-balance, separate basal drag laws for soft and hard beds, a few minor bug fixes, and changes to the iterative SSA solution to further optimize speed and numerical stability while allowing recovery from iterative convergence failures.

https://doi.org/10.5194/gmd-2024-175
Preprint. Discussion started: 17 January 2025

Geoscientific Model Development Discussions

The ice thermo-dynamics (section 2.6) is an energy-conserving finite-volume formulation (Patankar, 1980). The bed thermodynamics (section 2.6) resolves permafrost and includes corrections for seasonal snow cover over ice-free land (Tarasov and Peltier, 2007).

The GSM has an asynchronously coupled global visco-elastic isostatic response GIA solver (Tarasov and Peltier, 1997) with a linear approximation for geoidal deflection (section 2.15).

Surface drainage (section 2.8) is diagnostically resolved using a down-slope formulation that fills topographic depressions (lakes) while maintaining mass-conservation (Tarasov and Peltier, 2006). The resolving of pro-glacial lakes permits inclusion of a simplified lake ice parameterization (section 2.9) and a fresh-water calving component limited by available lake heat (section 2.7.5). Surface melt includes a novel positive degree solar insolation component (section 2.7.1). Subshelf melt uses a buoyant plume parameterization (section 2.7.2), while calving parametrically accounts for crack propagation and strain (section 2.7.3 and 2.7.4) enabling the capture of marine ice cliff instabilities.

For climate forcing, the GSM simultaneously uses glacially-indexed GCM snapshots and an asynchronously-coupled, geographically-resolved, energy balance climate model with non-linear snow and sea ice albedo feedback (section 2.10.2). Precipitation is subject to wind-climatology driven orographic forcing to account for the strong impact of orography (section 2.10.3).

Other optional components include several fully coupled basal hydrology representations (section 2.13 and Drew and Tarasov, 2023), a state-of-the-art subglacial sediment process model (section 2.14 and Drew and Tarasov, 2024), and a sub-grid hypsometric surface mass-balance and ice flow model to partly compensate for coarser grid resolution (section 2.11 and Le Morzadec et al., 2015). Relevant details on each component are provided in the indicated subsections.

2.1 GSM parameters

Any complex geophysical model will have a host of poorly constrained parameters that significantly impact model simulations. To address this, the GSM has a comparatively large set of ensemble parameters ((Tables 2 and 3) that define the parametric configuration for a given run. This is in contrast to “GSM parameters” denoting parameters set to fixed values based on physics or relative model insensitivity to the parameter (Table 4). The selection of the ensemble parameters has been refined during the course of decades of calibration and sensitivity analysis (e.g. Tarasov and Peltier, 2004; Tarasov et al., 2012).

While each paleo ice sheet will have some specific ensemble parameters, the majority of parameters are common across ice sheets. The majority of ensemble parameters are scaled to give a $0 \rightarrow 1$ input range. However, others that have a somewhat clearer physical interpretation may have a different scaling. To ensure a reasonably comparable scale, all ensemble parameters are subject to the following scaling rules. First the maximum value must be greater than or equal to 0 and less than 10. Second, the parameter range must be greater than 0.1. Some ensemble parameters (*e.g.,* h_{wbCrit} in Tables 2) may be scaled exponentially to permit a nominal $0 \rightarrow 1$ range.

https://doi.org/10.5194/gmd-2024-175
Preprint. Discussion started: 17 January 2025

Geoscientific Model Development Discussions
Open Access

Table 2. Non-climate forcing ensemble parameters. Input parameter ranges are given by the $(a \rightarrow b)$ specification with subsequent scaling/shifting as indicated. The sign in the response column indicates the typical LGM ice volume response to an increased value of the parameter based on sensitivity tests or a priori reasoning when straightforward. It should be noted that opposite responses are possible for some of the parameters depending on the whole parameter vector value. "LGM" is last glacial maximum.

Definition	Parameter	Code name	Response	Range and scaling
Weertman coefficient for soft-bed	C_{sb} (Eq. 10)	rmu	-	$(0.1 \rightarrow 2.0) \times 3$ km/yr $/(30kPa)^{m_s}$
sliding coefficient for hard bed	C_{hb} (Eq. 11)	fnslid	-	$(0.1 \rightarrow 4.0) \times 200$ m/yr $/(100kPa)^{m_h}$
Glen flow law enhancement	E_f	fnflow	-	subranges of $(1.5 \rightarrow 4.5)$ range depending on grid resolution
Coulomb-plastic friction coefficient	C_{Coul} (Eq. 6)	rCfrict	+	$(3.1 \rightarrow 4.5) - 3.0$ else 0
basal drag soft bed subgrid roughness dependency	$C_{\sigma\mathrm{sb}}$ (Eq. 10)	fSTDtill	+	$0.0 \rightarrow 2.0$
basal drag hard bed subgrid roughness dependency	$C_{\sigma\mathrm{hb}}$ (Eq. 11)	fSTDslid	+	$0.0 \rightarrow 2.0$
soft bed Weertman sliding exponent	m_s (Eq. 5)	POWbtill		$NINT((0.0 \rightarrow 1.0) \times 10)$
effective bed roughness scale	h_{wbCrit} (Eq. 50)	hwbCrit	+	$0.01 \times 10^{(2(0.0 \rightarrow 1.0))}$ m
constant bed drainage rate		rBedDrainRate	+	$10^{(0.0 \rightarrow 1.0)-3}$ m yr^{-1}
effective-pressure factor	C_{Neff} (Eq. 6)	rNeffFact	-	$2 \times 10^{4-(0.0 \rightarrow 1.0)}$ Pa
weight of first input deep geothermal heat flux map		wGF1		$0.0 \rightarrow 1.0$
Alternative till cover map weight		wtBedTill1		$0.0 \rightarrow 1.1$
calving coefficient	C_{calv} (Eq. 26 and 31)	fcalvin	-	$(0.1 \rightarrow 0.9) \times 10$ km/yr
hydrofracturing coefficient	C_{hydCrk} (Eq. 30)	pfactdwCrack		$(0.5 \rightarrow 4.0) \times 100$
calving face melt coefficient	C_{face} (Eq. 24)	CfaceMelt	-	$(0.5 \rightarrow 4.0) \times 10$
sub shelf melt coefficient	C_{SSM} (Eq. 22)	fSSMdeep	-	$(0.0 \rightarrow 1.0) \times 1.6 + 0.2$
marine freezing point (effective bias adjustment)	CT_{ssmCut} (Eq. 23 and 24)	TssmCut	-	$(0.0 \rightarrow 1.0) \times -4^oC$
lacustrine calving parameter		flac	-	$0.0 \rightarrow 0.4$
shortwave surface melt coefficient	C_{RadSMB} (Eq. 16)	fRadSMB	-	$(0.2 \rightarrow 0.5) \times 2$
thickness of the lithosphere	d_{L}			$(46 \rightarrow 146)$ km
viscosity of the upper mantle	η_{um}			$(0.1 \rightarrow 2.0) \times 10^{21}$ Pa s
viscosity of the lower mantle	η_{lm}			$(1.0 \rightarrow 50) \times 10^{21}$ Pa s
North America and Eurasia specific				
margin chronology weighting		wmargw		$0.0 \rightarrow 1.0$
margin forcing ablation threshold	F_m	margbab	-	$0.0 \rightarrow 1.0$
margin forcing accumulation threshold	F_a	margbac	+	$0.0 \rightarrow 1.0$
margin forcing calving reduction factor	F_c	margcalv	-	$0.0 \rightarrow 1.0$

https://doi.org/10.5194/gmd-2024-175
Preprint. Discussion started: 17 January 2025

Geoscientific Model Development
Discussions

Table 3. Climate forcing ensemble parameters. Parameter scalings follow the same rules as described in Table 2.

Definition	Parameter	Code name	Response	Range
weight of annual glacial index from ice core records		wtIndxYr		$0.0 \rightarrow 1.0$
weight of energy balance climate model (EBM) for glacial index setting		rWtEBMindx	-	$0.0 \rightarrow 1.0$
weight of EBM temperature field		fTweightEBM		$0.0 \rightarrow 1.0$
weight of glacially-indexed input GCM 2 meter temperature field		fTweightPMIP		$0.0 \rightarrow 1.0$
scaling of EBM temperature field glacial anomaly	C_{EBM} (Eq. 40)	fnTEBMscale	+	$0.8 \rightarrow 1.25$
global temperature index scale factor	C_{IT} (Eq. 35)	fnTdfscale	+	$0.85 \rightarrow 1.2$
temperature glacial index exponent	Θ_T (Eq. 35)	fnTdexp	-	$0.85 \rightarrow 1.4$
LGM temperature EOF components		fTEOF[NvTEOF]		$(0.0 \rightarrow 1.0) - 0.5$
LGM vertical air temperature gradient		rlapselgm	-	$(0 \rightarrow 1) \times 4 + 4\,^{o}C/$ km
glacial index boost where ice cover	$I_{\mathrm{H+}}$ (Eq. 43)	HboostTndx		$0. \rightarrow 0.2$
weight of glacially-indexed input GCM precipitation field		fPREweightPMIP		$0.0 \rightarrow 1.0$
global precipitation scale factor for PMIP component	C_{pre} (Eq. 44)	fnpre	+	$0.6 \rightarrow 1.8$
LGM precipitation EOF components		fPEOF[NvPEOF]		$(0.0 \rightarrow 1.0) - 0.5$
precipitation orographic forcing regularization	μ_p (Eq. 47 and 48)	pREG		$0.0 \rightarrow 1.0$
coefficient for exponential surface temperature dependence of non-PMIP precip	C_{Tp}(Eq. 45	hpre	-	$0.0 \rightarrow 1.0$
precipitation glacial index phase exponent	Θ_P (Eq. 44)	fnPdexp		$0.4 \rightarrow 2.0$
desert elevation control parameter	h_{Ides} (Eq. 36)	rtdes		$0.0 \rightarrow 1.0$
desert-elevation exponent	C_{des} (Eq. 46)	desFac	-	$0.5 \rightarrow 2.5$
default desert-elevation cutoff	h_{des0} (Eq. 46)	des2	+	$0.0 \rightarrow 2.0$ km
ocean temperature glacial index phase factor	Θ_{TO}	rToceanPhase		$0.5 \rightarrow 2.0$
negative glacial index ocean warming enhancement factor		rToceanWrm		$0.0 \rightarrow 1.0$
North American specific				
South central precipitation enhancement		fmpreSM	+	$0.0 \rightarrow 1.0$
western desert-elevation cutoff		desW	+	$0.2 \rightarrow 3.0$ km
northwestern desert-elevation cutoff		desNW	+	$0.0 \rightarrow 2.0$ km
north-central desert-elevation cutoff		desNC	+	$0.0 \rightarrow 1.5$ km
central desert-elevation cutoff		desC	+	$0.0 \rightarrow 2.0$ km
Foxe Basin/Baffin desert-elevation cutoff		desF	+	$0.0 \rightarrow 2.0$ km
Quebec/Labrador desert-elevation cutoff		desQ	+	$0.0 \rightarrow 3.0$ km
midsouth-central desert-elevation cutoff		desScN	+	$0.0 \rightarrow 2.4$ km
south-central desert-elevation cutoff		desSC	+	$0.0 \rightarrow 2.0$ km
Greenland specific				
latitudinal ramp width of added Holocene warming	Θ_{wrm} (Eq. 42)	yTagDx		$42. - 40 \times (0.0 \rightarrow 1.0)$
Holocene warming scale	CHTM (Eq. 42)	fTag		$0.0 \rightarrow 1.0$
Eurasian specific				
added regional summer warming scaling for EBM		rSumPlusEBM	-	$(0.0 \rightarrow 1.0) + 0.5$
British Isles desert-elevation cutoff		desBA	+	$0.0 \rightarrow 2.0$ km
Fennoscandian desert-elevation cutoff		desFS	+	$0.0 \rightarrow 2.0$ km
Barents-Kara desert-elevation cutoff		desBK	+	$0.0 \rightarrow 2.0$ km
Antarctic specific				
Regional subshelf ocean temperature shift		TregSSMCut(0:6)	-	$(0.0 \rightarrow 1.0) \times 4$

https://doi.org/10.5194/gmd-2024-175
Preprint. Discussion started: 17 January 2025

Table 4. default GSM (non-ensemble) parameters, symbols, and grid specification

Definition	Parameter	Value
Earth radius	r_e	6370 km
Earth mass	m_e	5.976×10^{24} kg
acceleration due to gravity	g	$9.81\ ms^{-2}$
water latent heat of fusion	L_w	$3.35 \times 10^5\ J\ kg^{-1}$
ocean water density	ρ_s	$1028\ kg\ m^{-3}$
ice density	ρ_i	$910\ kg\ m^{-3}$
ice specific heat capacity	$c_i(T)$	$(152.5 + 7.122 \cdot T)\ J\ kg^{-1}\ K^{-1}$
ice thermal conductivity	$k_i(T)$	$9.828 \cdot \exp(-0.0057 \cdot T)\ W\ m^{-1}\ K^{-1}$
bedrock density	ρ_b	$3300\ kg\ m^{-3}$
bedrock specific heat capacity	c_b	$1000\ J\ kg^{-1}\ ^{\circ}\mathrm{C}^{-1}$
bedrock thermal conductivity	k_b	$3\ W\ m^{-1}\ ^{\circ}\mathrm{C}^{-1}$
number of ice dynamic levels	nz_i	12
number of ice thermodynamic levels	nz_{Ti}	65
number of bed thermodynamic levels	nz_{Tb}	16
Glen flow law coefficient, $T < -10^o$ C	A_c	$8.9836 \times 10^{-6}\mathrm{Pa}^3\mathrm{yr}^{-1}$
Glen flow law coefficient, $T > -10^o$ C	A_w	$7.43377 \times 10^{5}\mathrm{Pa}^3\mathrm{yr}^{-1}$
creep activation energy of ice, $T < -10^o$ C	Q_c	$6 \times 10^4\mathrm{Jmol}^{-1}$
creep activation energy of ice, $T > -10^o$ C	Q_w	$1.15 \times 10^5\mathrm{Jmol}^{-1}$
Glen flow law exponent	n	3
minimum till friction angle	ϕ_{min}	10^o
maximum till friction angle	ϕ_{max}	30^o

2.2 GSM grid and structure

The GSM is mostly coded following Fortran 90 conventions and formatting, including the use of modules and implicit none (a few legacy components, including the coupled energy balance climate model (EBM) have yet to be brought to this standard). Numerous configuration options are under compile flag control.

The GSM has an ice sheet index dimension allowing separate ice sheet domains instead of, for instance, requiring a grid covering the whole globe. There are 3 horizontal grid options: regular dx,dy; regular longitude,latitude; and polar stereographic projection. The vertical grid is a standard sigma grid for ice temperature with default 65 layers (GSM parameter NCZ), and an irregularly spaced sigma grid for vertical velocities (with default NLEV= 12 layers and high resolution near the bed). As is fairly standard, the ice sheet model uses an Arakawa C-grid, with fluxes and velocities computed on grid cell interfaces.

The bed thermodynamic grid has exponential spacing in accordance with diffusion scaling. It has a default 26 layers (GSM parameter NTBZ) and scaling exponent value of 1.21 (GSM parameter RbedSCALE) for a default 4 km deep bed.

https://doi.org/10.5194/gmd-2024-175
Preprint. Discussion started: 17 January 2025

2.3 A caveat on parameterizations in the GSM

Given the breadth of applications the GSM has, or is, being used for (all last glacial cycle ice sheets from Icelandic to Antarctic), and the dimension of the ensemble parameter space and range of climate inputs used; there is no such thing as an optimal parameterization. A further complication is the over two decades of continuous development. Optimal fits from earlier GSM versions may no longer be optimal given changes in input topographies, climate inputs, etc... As such, the approach has been to combine physical reasoning, parametric forms from the literature, and broaden degrees of freedom across various components to albeit incompletely convert process uncertainties into ensemble parameter uncertainties.

2.4 Ice dynamics

The hybrid SSA/SIA solver was imported from Pollard and DeConto (2012) and thereby uses the identical finite difference discretization. This discretization naturally imposes the appropriate boundary condition for a floating ice margin. Aside from conversion to F90 standard, the main change after import was the insertion of a sequence of matrix solver options for the SSA equations in case of convergence failure. First, a biconjugate gradient squared solution (BCGS option for the NSPCG solver) is attempted. Upon failure, a generalized minimal residual (GMRES) solution is subsequently attempted. Upon further failure, successive over relaxation (SOR) will be tried. The first two options use a symmetric successive over-relaxation preconditioner (SSOR). If convergence failure persists, the GSM steps back to the beginning of the last dlong interval (default 100 years) and the time-stepping is repeated with half the ice dynamical time-step ($delt$). The short time-step is retained for at least three hundred years and then reverts back to the previous value when permitted by the CFL (Courant–Friedrichs–Lewy) criterion.

The solution of the hybrid SSA/SIA equation involves an outer Picard loop (1:NITERC) for ice thickness and a sequence of two inner loops (1:NITERA) to solve the SSA elliptic equations for the horizontal ice velocities (cf appendix A1), first without the grounding line flux condition, then with it. Default convergence thresholds are 0.5% and 2 m/yr respectively for the maximum grid cell residuals between successive iterations. For the default compile flags, the outer Picard iteration is subject to 10% damping of the first iteration (-DNumDamp) and to the unstable manifold correction of Hindmarsh and Payne (1996) for all but the last iteration (-DHPiterc). Sensitivities to these numerical compiler flag options for example GRIS and AIS glacial cycle simulations are in appendix B.

The default choice for the stopping criteria for the SSA elliptic matrix solution (say of the form $\mathbf{Au} = \mathbf{b}$) is the relative norm (option 10 of the NSPCG package, Kincaid et al., 1989) of the left pre-conditioned residual $\mathbf{z}$ (for preconditioner Q):

$$\left[\frac{||\mathbf{z}||}{||\mathbf{Q_L^{-1}b}||}\right] < \zeta \tag{1}$$

where

$$\mathbf{z} = \mathbf{Q_L^{-1}}(\mathbf{b} - \mathbf{Au}) \tag{2}$$

Convergence thresholds (ζ) are a function of the iteration, with final iteration thresholds of 1×10^{-5} or smaller.

In addition to the default grounding line ice flux treatment of Schoof (2007) for Weertman type sliding, we've added a Coulomb-plastic option from Tsai et al. (2015). The grounding-line ice thickness for the flux calculation is determined via a

https://doi.org/10.5194/gmd-2024-175
Preprint. Discussion started: 17 January 2025

Geoscientific Model Development
Open Access
Discussions
EGU

subgrid interpolation as in Pollard and DeConto (2012). The treatment of 2D buttressing effects on grounding line fluxes in the GSM has been revised as per Pollard and DeConto (2020). This addresses limitations of the original (Pollard and DeConto, 2012) approach when compared against the results of an Antarctic ice sheet model with a highly resolved computational mesh around grounding lines (Reese et al., 2018).

The only other significant ice dynamical differences from Pollard and DeConto (2012) are the specification of basal drag and basal sliding activation as detailed below (section 2.5) and a correction to handle floating ice grounding onto ice free land.

The default Glenn flow law dependence on ice temperature follows the recommended values of Cuffey and Paterson (2010). An ensemble parameter (E_f) provides the default flow enhancement. The basal ice layer in the model is given an extra 50% enhancement to partly capture the observed lower effective viscosity of older basal ice (Cuffey and Paterson, 2010). As well, the enhancement in the upper half of the ice column is reduced by 50% to partly account for the reduced fabric development in younger ice (Cuffey and Paterson, 2010).

Ice flow enhancement in the GSM also partially accounts for anisotropic effects from fabric development in polar ice (Ma et al., 2010). This fabric development tends to stiffen the ice with respect to horizontal strain. As the traditional Glenn flow law enhancement factor in good part represents the enhancement in vertical shear due to this fabric development, it stands to reason that for horizontal strain, this factor should take on some sort of inverse relation to the SIA enhancement. Invoking Occam's razor, along with the requirement that the SSA enhancement $E_{shelf}(E_{SIA}=1)=1$ and $E_{shelf}(E_{SIA}=5.6)=0.6$ from Ma et al. (2010), the SSA enhancement factors are set to

$$E_{shelf} = 0.48696/E_f + 0.51304 \tag{3}$$

for ice shelves. For ice streams, Ma et al. (2010) recommend a value of 1 at the onset, and the ice shelf value at the grounding line. To avoid the required relative position tracking, an average value of

$$E_{stream} = 0.5 \cdot (E_{shelf} + 1.0) \tag{4}$$

is applied.

2.5 Basal drag

Given the uncertainties in the appropriate form of the large scale basal drag law for soft bed (*e.g.,* Fowler, 2003), the GSM has both Weertman power law and Coulomb plastic options for soft-bedded basal drag. For the Weertman case, the effective basal sliding law (for both hard or soft beds) is given by:

$$\boldsymbol{U_b} = C_b \, |\boldsymbol{\tau_b}|^{m_b-1} \, \boldsymbol{\tau_b} \tag{5}$$

for basal drag $\boldsymbol{\tau_b}$ and basal velocity $\boldsymbol{U_b}$. C_b incorporates a basal temperature ramp for sliding activation (for a detail examination surge cycling response to the form of this ramp cf Hank et al., 2023). C_b also accounts for: potential subgrid warm based conditions in topographic lows, bed type (soft or hard), and drag reduction under pinned shelf conditions (as detailed below).

https://doi.org/10.5194/gmd-2024-175
Preprint. Discussion started: 17 January 2025

The exponent (m_b) is generally treated as an ensemble parameter ($m_b = m_s$ in Table 2) when the bed has deforming till cover given the range of inferred values in the literature (*e.g.,* Gillet-Chaulet et al., 2016; Maier et al., 2021).

With the -DNeffDRAG compile flag and any form of basal hydrology, the Weertman basal sliding coefficient is multiplied by

$$\min(10., \max(0.2, \frac{C_{\text{Neff}}}{N_{\text{eff}} + N_{\text{reg}}})) \tag{6}$$

where N_{eff} is the computed effective basal pressure (cf section 2.13), $C_{N_{\text{eff}}}$ is an ensemble parameter scaling coefficient, and the regularization parameter N_{reg} has value 10 kPa.

Based on the results of a basal drag inversion for Greenland (Maier et al., 2021), the hard bed has a default power law exponent $m_b = 4$ but otherwise has the same form of Weertman type sliding law as for soft-bedded Weertman (eq. 5).

For Coulomb plastic basal drag, a regularized form has been found to have better numerical convergence:

$$\boldsymbol{\tau_b} = \max\left(1kPa\ ,\ N_{\text{eff}}\, C_{\text{Coul}}\ \tan(\theta_t)\ \left(\frac{\boldsymbol{U_b}^2}{\boldsymbol{U_b}^2 + U_{\text{sqReg}}}\right)^{1/6}\right) \tag{7}$$

where C_{Coul} is a drag coefficient, U_{sqReg} is a regularization velocity term ($(20\,m/yr)^2$) and θ_t is the elevation dependent friction till angle (as per Maris et al., 2014) to account for the increased prevalence of saturated fine sediment cover in marine sectors:

$$\phi = \begin{cases} \phi_{min} = 10^o & h_{\text{bG}} \leq -10^3, \\ \frac{-h_{\text{bG}}}{10^3} \cdot \phi_{min} + (1 + \frac{h_{\text{bG}}}{10^3}) \cdot \phi_{max} & -10^3 < h_{\text{bG}} \leq 0, \\ \phi_{max} = 30^o & h_{\text{bG}} > 0 \end{cases} \tag{8}$$

where h_{bG} is the bed elevation relative to contemporaneous sea level. This formulation uses an appropriate linearization around the previous value of the basal velocity (U_b^*) in the iterative solution of the SSA velocity equation:

$$\boldsymbol{\tau_b} = \boldsymbol{\tau_b^*} + \frac{\partial \boldsymbol{\tau_b^*}}{\partial \boldsymbol{U_b^*}} \cdot (\boldsymbol{U_b} - \boldsymbol{U_b^*}) \tag{9}$$

If the computed Coulomb plastic basal drag is greater than the Weertman basal drag (pre-computed using an SIA approximation for drag law selection only), then the latter basal drag law is used instead. This has both a physical motivation (at high effective pressure and warm-based conditions, Weertman sliding is plausible, *e.g.,* Tsai et al., 2015), and a numerical motivation (ensuring the basal drag is never larger than the sum of remaining horizontal stresses).

The two Coulomb plastic options are more numerically unstable, and as such, a high exponent Weertman law (*e.g.,* exponent 7) is recommended in lieu when computational resources are a limiting factor.

2.5.1 Basal drag geological and subgrid topographic controls

The determination of soft/hard bed is set according to whether the fractional soft bed cover of the grid cell is above or below GSM parameter SEDCUT (default 0.5). A future improvement will be the inclusion of fractional basal drag from both hard/soft bed components. As the basal drag is computed at grid cell interfaces, the sediment fraction at the interface must be set. This is taken as the square root of the product of adjacent sediment cover fractions in partial accord with a numerically self-consistent treatment for the setting of cell interface diffusion coefficients (the square root operation was chosen to provide an intermediate between an arithmetic mean and the numerically appropriate regularized harmonic mean for a linear diffusion process, cf Patankar, 1980).

One to date unresolved issue is how to deal with fractional and thin till cover as well as the impact of different classes of sediments. The default approach in the GSM is to set the local sediment fraction coefficient (sedF in eqs. 10 and 11) to the minimum of 1.5 and $2\times$ the input sediment fraction for regions that are presently marine and otherwise to the input value raised to the power of the ensemble parameter fbedpow. This is intended to crudely account for the likely lower drag from marine muds and otherwise provide some ensemble parametric control.

Another unresolved issue for basal drag is the appropriate accounting for the impact of subgrid bed roughness. Presumably a rougher bed will increase basal drag, with bedrock exposures acting as pinning points. However an opposing mechanism could also be argued with a rough hard bed promoting the trapping of subglacial sediment. Though there have been some detailed relationships proposed based on single basin scale analysis (*e.g.,* Wilkens et al., 2015), their validity for continental scale applications are unclear and furthermore their data input requirements are unlikely to be met for the global ice sheet context in the foreseeable future. To address some of these uncertainties, in addition to ensemble separate parameter sliding coefficients for hard and soft beds (C_{sb} and C_{hb}), two ensemble parameters ($C_{\sigma\mathrm{sb}}$, $C_{\sigma\mathrm{hb}}$) impose Weertman basal drag dependencies on the subgrid standard deviation of bed elevation (σ_b in m). For soft beds, this takes the form of a basal sliding coefficient:

$$C_B = C_{\mathrm{sb}} \cdot \mathrm{sedF} \cdot \min(1, \max(0.2, C_{\sigma\mathrm{sb}}/(0.01\,\sigma_b))) \tag{10}$$

For hard beds, an adhoc term accounting for the subgrid fraction of soft bed cover (sedF) is also included:

$$C_B = C_{\mathrm{hb}} \cdot (1. + 20.\,\mathrm{sedF}) \cdot \min(1.0, \max(0.1, C_{\sigma\mathrm{hb}}/(0.01\,\sigma_b))) \tag{11}$$

The GSM has not been setup for present-day inversion of a basal drag map for existing ice sheets. For paleo contexts, such inversions are problematic given the confounding impacts of changes in basal water pressure and basal sediment thickness. Nor can such inversions provide a value where the bed is currently frozen. A last motivation for this design choice is to encourage the development of basal drag parameterizations that can be applied to all paleo ice sheets, be it for regions that are presently subglacial, marine, or subaerial.

A key issue for ice shelf modelling is the presence of potential subgrid pinning points under the ice shelf that aren't presently active. This is a significant source of uncertainty given the lack of detailed topographic data for the subshelf environment. To partly address this, the model has a standard option of assuming a Gaussian distribution of subgrid pinning points based on a map of the standard deviation of the subgrid bed elevation. For poorly observed regions, adjacent open marine environments can provide an estimate when creating these maps. The pinning point effect is simply imposed as a fractional coefficient (fpin<1) that multiplies the basal drag derived as if the shelf was grounded. fpin is set to the cumulative normal distribution (more exactly an analytical approximation thereof) for subgrid elevation above the distance between the bed and ice shelf base.

For distances of more than 3 standard deviations of basal roughness, fpin is effectively set to 0 (an unpinned ice shelf with a very small basal drag (0.001 Pa/(m/yr)) to avoid singularities in the stress balance matrix).

2.5.2 Basal sliding activation

A key issue that most ice sheet models do not explicitly address is the appropriate activation function for basal sliding as warm-based conditions are approached. A detailed resolution scaling analysis of this issue has recently been published (Hank et al., 2023), and its recommended activation function is under compile flag choice (-DTrampScN). Briefly this is implemented via an estimated warm-based fraction of a grid cell F_{warm} (also indirectly accounting for sub-temperate sliding, eg. Fowler, 1986):

$$F_{\mathrm{warm}} = \max\left[0, \min\left(1, \frac{T_{\mathrm{bp,I}} + T_{\mathrm{ramp}}}{T_{\mathrm{ramp}}}\right)\right]^{T_{\mathrm{exp}}}, \tag{12}$$

where $T_{\mathrm{bp,I}}$ is the grid cell interface basal temperature relative to the pressure melting point, T_{ramp} is the temperature interval for which the grid cell has some warm-based subgrid ice, and T_{exp} the exponent used for the ramp. This ramp depends on the subgrid standard deviation of elevation (σ_{hb}, in metres) given that a higher standard deviation can increase the subgrid fraction at the pressure melting point when the nominal grid cell basal temperature is below the pressure melting point. As such and with explicit dependence on grid cell resolution (Δxy), T_{ramp} is given by:

$$T_{\mathrm{ramp}} = \max(1.0\ ,\ 0.02\,\sigma_b) \cdot \frac{\Delta xy}{50\ \mathrm{km}}\ {}^{\circ}\mathrm{C} \tag{13}$$

This choice of resolution dependence (as determined in Hank et al., 2023) leads to a sharper temperature ramp for finer horizontal grid resolutions, as would be expected on physical grounds (since the range of subgrid basal temperatures for a grid cell, when not fully warm-based, will generally be larger for a larger grid cell). The subgrid warm-based fraction F_{warm} then enters into the basal drag coefficient C_b (cf eq 5) as following:

$$C_b = \max(F_{\mathrm{warm}} \cdot C_B\ ,\ C_{\mathrm{froz}})\,. \tag{14}$$

C_{froz} is the fully cold-based sliding coefficient for numerical regularization:

$$C_{\mathrm{froz}} = 2 \cdot 10^{-4}\ \mathrm{m\ yr^{-1}} \left(5 \cdot 10^{-6}\ \mathrm{Pa^{-1}}\right)^{m_b}. \tag{15}$$

The detailed analysis of ice sheet model sliding activation specification in Hank et al. (2023) focused on surge cycling in an idealization of Hudson Bay and Hudson Strait. It did not consider other paleo ice sheets. For an example GRIS simulation, the ice volume response to the width of T_{ramp} in eq. 12 is very strong (Fig. 1), especially when compared to the minimal response to other numerical compiler flags (Fig. B1). It is also one of the more sensitive numerical flags for an example AIS simulation (Fig. B2). This further underlines the importance of a numerically and physically justified specification of basal sliding activation.

Another non-trivial issue for ice sheet models with continental scale grids is the appropriate determination of the basal interface temperature. The preferred approach in the GSM accounts for the potential warming at the warm-cold interface by

https://doi.org/10.5194/gmd-2024-175
Preprint. Discussion started: 17 January 2025

Geoscientific Model Development
Discussions

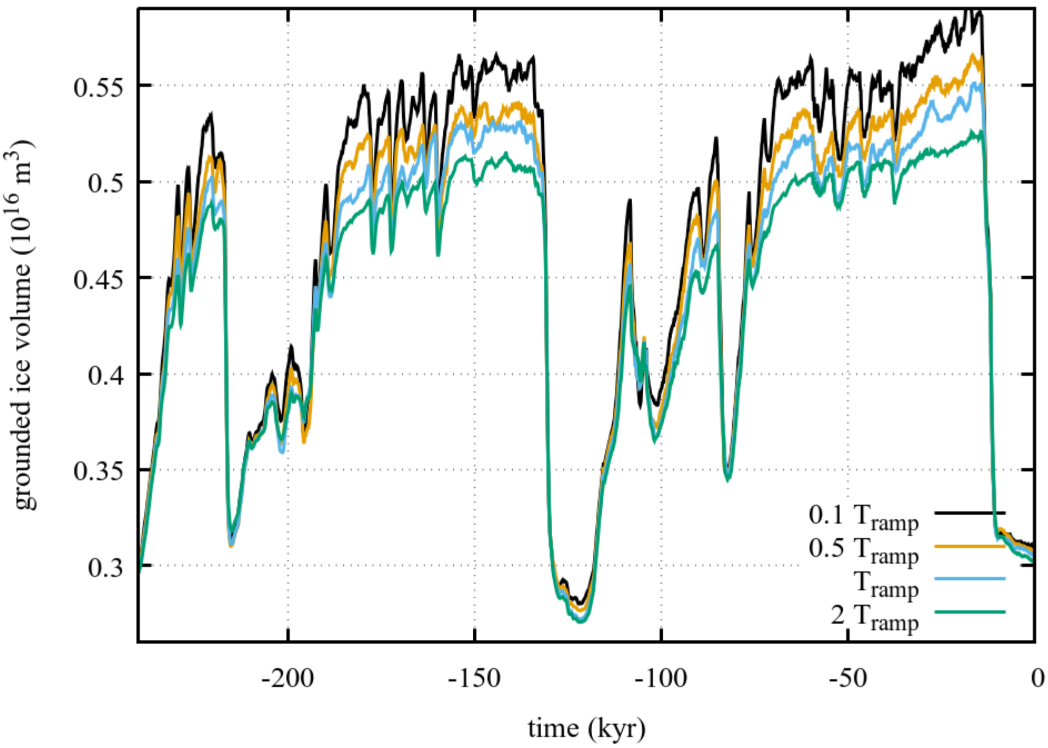

Figure 1. Example GRIS ice volume history sensitivity to the width of the basal sliding activation temperature ramp (T_{ramp}) in eq. 12. The simulations use the default 0.5^o by 0.25^o (longitude, latitude) resolution.

refreezing of subglacial meltwater. This is approximated (with -DTbpmGbI) by using half of the latent heat flux embodied in subglacial meltwater generated by the two grid cells bordering the cell interface under question. This latent heat is distributed across the basal ice dynamical layer to convert to a temperature increment and added to the interpolated basal temperature at the interface. Hank et al. (2023) provides a detailed description and comparison of this and alternative treatments for computing the basal temperature at the grid cell interface.

2.6 GSM ice and permafrost resolving bed thermodynamics

The GSM finite volume thermodynamic scheme uses an implicit solution for the vertical and local components and explicit solution for the horizontal advection component of the energy conservation equation:

$$\rho_i c_i(T(\mathbf{r}))\frac{\partial T(\mathbf{r})}{\partial t} \quad = \quad \frac{\partial}{\partial z}\left(k_i(T(\mathbf{r}))\frac{dT(\mathbf{r})}{dz}\right) - \rho_i c_i(T(\mathbf{r}))\mathbf{V}(\mathbf{r})\cdot\nabla T(\mathbf{r}) + Q_d(\mathbf{r})\,.$$

https://doi.org/10.5194/gmd-2024-175
Preprint. Discussion started: 17 January 2025

Heat source terms include full SSA and SIA contributions to deformation work (Q_d) and the boundary heat flux from basal sliding.

Horizontal advection is discretized using a second-order interface consistent 3 pt upwinding. Vertical diffusion and advection is solved implicitly using the power-law finite volume treatment of Patankar (1980). Interface diffusivities are based on geometric means as per ibid.

The discretization of the basal ice grid cell is non-standard to enable solution for the temperature at the basal interface with the bed thermal model. To do so, horizontal advection and the time derivative use a grid-cell centre temperature that is linearly interpolated to the base.

For thin ice ($H < 50$ m), basal temperature is set to that of the highest elevation neighbouring grid cell with ice thickness > 50 m, and ice temperature is linearly interpolated in the vertical from the bed to surface. If there is no appropriate neighbour, the whole ice column is set to mean annual surface temperature. For floating ice, the basal temperature is set to the pressure melting point.

Unlike many ice sheet models, energy is conserved when a grid-cell reaches the pressure-melting point. This is accomplished via an extra iteration within the tri-diagonal solution of the implicit energy conservation solution. The residual heat is then used for basal melt. The vertical implicit solution is over the whole ice and bed grid. Thermodynamic time-stepping is subject to horizontal CFL constraints using time-interpolated horizontal ice velocities. Though the vertical solution is implicit, this does not mean that the solution will have no time-step sensitivity. As such, the solver includes a vertical sub-iteration to restrict the time-step for any single vertical column to a set factor of the CFL stability threshold. This sub-iteration time-step factor has a default value of 10 (chosen on the basis of sensitivity tests) but is adjusted as needed to impose a maximum of 100 sub-iteration time-steps.

As is standard given space-time scales, the bed thermodynamics assumes vertical diffusive heat transport only. What is much less common is that it accounts for permafrost via a standard heat capacity approximation (Osterkamp, 1987; Williams and Smith, 1989; Mottaghy and Rath, 2006). It also applies temperature forcing corrections at the top of subaerial frozen ground to partly account for the effects of seasonal snow cover and surface vegetation (Smith and Riseborough, 2002). The GSM thermal bed has a default depth (GSM parameter BEDTdepth) of 4 km for which the lower flux boundary condition is specified by an input map (section 2.17). A challenge in this regard is the lack of a confident inversion for the global geothermal heat flux at such a depth. A comparison of results for an older version of the GSM (but with the same bed thermal model) against North American deep borehole temperature profiles along with a full description of the bed thermal model are in Tarasov and Peltier (2007).

The default coupling between GSM ice dynamics and thermodynamics is explicit with a minimum one year time-step. However, the GSM includes an option for an iterative implicit coupling solution (-DimplicCoupleDynTherm). The implicit coupling iteration is for each ice dynamical time-step. It is subject to a chosen convergence threshold for both maximum ice thickness and horizontal velocity component differences between successive iterations.

https://doi.org/10.5194/gmd-2024-175
Preprint. Discussion started: 17 January 2025

Geoscientific Model Development Discussions

2.7 Mass balance processes

Mass balance process representation was chosen based on space-time resolution of required inputs and associated uncertainties.

2.7.1 Positive degree day and positive temperature insolation surface melt (PDDsw) and refreezing

The GSM uses a novel extension of the classical positive degree day (PDD) scheme that accounts for the changing short wave (SW) component of the surface energy-balance. PDD schemes (*e.g.,* Cuffey and Paterson, 2010) traditionally use two constant melt coefficients to crudely account for the changing albedo between ice and snow. However, it is well known that ice and snow albedos continuously vary. Furthermore, experiments with full surface energy balance models have made clear that orbital changes in short-wave forcing significantly affect surface mass-balance (van de Berg et al., 2011). From a physical point of view, PDD's are effectively a way to account for the long-wave, latent heat, and sensible heat flux components of surface energy balance (as all these fluxes depend on air temperature), but they do not account for variations in net short-wave fluxes beyond the binary choice of snow and ice PDD melt coefficients.

Observationally, fitted PDD melt coefficients vary over a wide range. We ascribe these variations in large part to changing mean net SW inputs and therefore choose a near lowest observationally-inferred value 3.3 mm/PDD (ice equivalent) for a single PDD coefficient (*e.g.,* Braithwaite, 1995; Hock, 2003) to capture the non-SW energy flux components. This value is a bit larger than that which would be inferred on the basis of pure long-wave and sensible energy balance to account for latent heat contributions.

For the shortwave component, a key challenge is that the short-wave input only contributes to surface melt if the surface temperature is at 0^o C. This constraint is often accounted for in present-day contexts for which hourly temperature and surface energy flux observations from automatic weather stations are available (*e.g.,* Irvine-Fynn et al., 2014). However, for paleo ice sheet modelling contexts, typically only monthly mean temperature climatologies are available. As such, short of the few coupled ice sheet and climate models able to do full energy balance calculations (*e.g.,* Krapp et al., 2017; Willeit et al., 2022), this constraint has not been applied in paleo ice sheet modelling contexts.

A possible computationally efficient solution to imposing this constraint arises from the similarity of the above temperature threshold to that of the contribution of PDDs to surface melt. Just as PDDs are computed for paleo modelling contexts based on a probabilistic distribution around mean monthly temperatures, a positive temperature time integrated surface insolation flux may also be computed. This requires an assumption relating near surface air temperature to actual snow/ice surface temperature. Though not identical we assume that on a time integrated basis, errors resulting from imposing the 0^o C constraint on air temperature are relatively minor compared to other sources of error. The GSM uses a statistical model for the shortwave insolation for 2 meter air temperature above 0^o C (S_{wrm}) as a function of mean monthly: solar insolation, number of PDDs per day (PDDd), and standard deviation of air temperature $\sigma_{T_{2m}}$. The model was derived from regression of mid to high latitude 4 hourly insolation and 2 meter air temperatures from the PLASIM GCM (Fraedrich, 2012) over a deglacial transient run (Andres and Tarasov, 2019) and takes the form:

$$S_{wrm} = \sqrt{\min(1.0, C_{\text{RadSMB}} \cdot \text{PDDd}/\sigma_{T_{2m}})} \cdot (1 - \text{albedo}) \cdot (\text{mean monthly surface insolation}) \quad (16)$$

https://doi.org/10.5194/gmd-2024-175
Preprint. Discussion started: 17 January 2025

Geoscientific Model Development Discussions

This regression captures much of the source GCM data signal (Fig. 2) with residual differences likely dominated by the lack of accounting for variations in cloud cover. The GSM surface insolation solution also accounts for orbital dependence and atmospheric transmissivity dependence on mean monthly solar angle (using the formulation of Irvine-Fynn et al., 2014).

To partially address the sensitivity to unresolved cloud cover, a cloud radiative transmissivity factor (GSM parameter CloudFactor) enables ice sheet scale adjustments. This factor is currently set to 0.7 with one exception. Based on initial ensemble modelling and motivated by the high observed frequency of cloud cover, the factor for Iceland is set to 0.4. The C_{RadSMB} ensemble parameter (eq 16) also provides an ice sheet scale ensemble parameter to partly address remaining uncertainties.

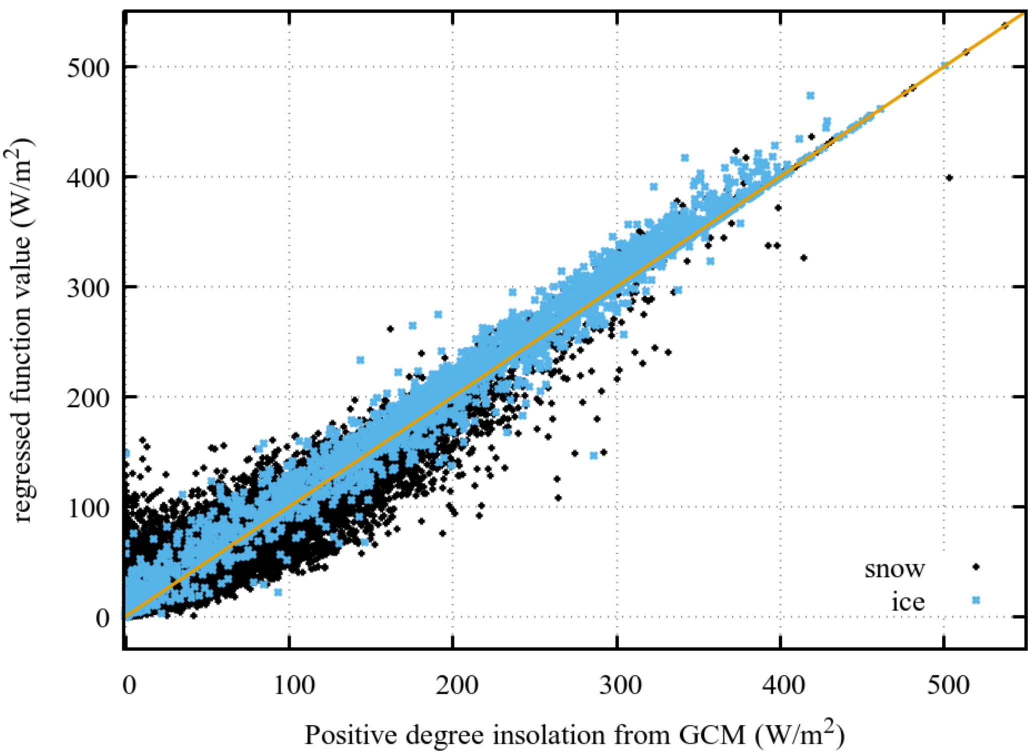

Figure 2. Comparison GCM computed and regressed function used in GSM for monthly mean of positive degree daily surface insolation. Results are disaggregated for snow and ice surfaces for ensemble parameter C_{RadSMB} in eq. 16 set to it's nominally regressed value of 0.345.

Surface albedo (using the recommended -DalbT2m compile flag) is a continuous function (Gabbi et al., 2014) of the nominal daily maximum 2 m air temperature ($T_{2\mathrm{max}}$). This is approximated as a function of mean monthly 2 m air temperature ($\overline{T_{2m}}$)

https://doi.org/10.5194/gmd-2024-175
Preprint. Discussion started: 17 January 2025

and standard deviation (σ_{T2m}) thereof:

$$T_{2\mathrm{max}} = \max(1.0, \overline{T_{2m}} + 1.4 \cdot \sigma_{\mathrm{T2m}}) \tag{17}$$

$$\mathrm{albedo} = 0.86 - 0.155 \cdot \log(T_{2\mathrm{max}}) \tag{18}$$

To date, it has been common for paleo ice sheet models to determine PDD as a function of mean monthly temperature assuming a Gaussian distribution with constant standard deviation. However, an examination of hourly temperature data from Greenland stations indicates this to be quite inaccurate (Wake and Marshall, 2015). As such, for computing PDDs, the GSM uses a observationally-fitted non-Gaussian distribution as a function of mean monthly temperature that was tested for various sites across Greenland, Norway, and Antarctica (Wake and Marshall, 2015). When coupled to full climate models, the GSM can instead take the monthly grid-cell standard deviation from the climate model.

The GSM uses a surface meltwater refreezing scheme that approximately accounts for firn meltwater retention and available refreezing potential. In detail, the model sets the thickness of annual superimposed (refrozen) ice (supice, with effective sum over repeated melt/refreeze in year) to

$$H_{\mathrm{act}} = \min(\ \mathrm{dFRZ},\ H + 0.5 \cdot \mathrm{accum}_{\mathrm{year}}) \tag{19}$$

$$\mathrm{supice} = \min(H_{\mathrm{act}} \cdot C_{\mathrm{ice}} / L_{\mathrm{ice}} \cdot \mathrm{NDY},\ \text{total snow melt and rain over year},\ 1.6\,\mathrm{accum}_{\mathrm{year}}\ ) \tag{20}$$

where NDY is the mean number of negative degree years computed in a similar approach to PDDs (or equivalent to $\mathrm{PDD}/365 - T_{2\mathrm{mmeanyear}}$). The maximum thermodynamically active depth dFRZ is set to 3.675 m (ice equivalent) based on loose tuning to present-day RACMO2.3p2 results for Greenland (Noël et al., 2018) and respecting bounds in Reijmer et al. (2012). The first term in the above supice equation sets the available freezing potential, the second term is the available supply of water for refreezing, and the third term the available pore space for trapping meltwater (set to the maximum modelled value for present-day Greenland for both RACMO2 and MAR RCMs in Reijmer et al., 2012). This parameterization deviates from previous in imposing the firn retention as a limiting factor instead of an additive refreezing term. This is justified based on the poorer fits of meltwater refreezing models with the additive firn retention term to RACMO2 and MAR RCM surface mass balance results for Greenland (ibid). Unfrozen meltwater will also be retained in any ice surface grid-cell scale depressions when the surface hydrology solver is active in the GSM.

The determination of monthly mean rain/snow fraction uses the monthly mean positive degree fraction for near surface air temperature. To better reflect that this fraction tends to be physically determined well above the surface, this fraction is computed relative to PDCUT$= 2^o$C. However, if there is evidence for a prevalence of temperature inversions during precipitation, this reference value should be lowered.

To partially account for the reduced variance of hourly temperature during cloudy days, a Gaussian distribution with a reduced effective standard deviation (σ_{PDf}, as compared to that of Wake and Marshall, 2015, used for the PDD determination) is used for the positive degree fraction. We use the observational fitted value of Seguinot and Rogozhina (2014):

$$\sigma_{PDf} = -0.15 \cdot T_{2m} + 1.66\,. \tag{21}$$

Though precipitation, PDDs, and NDYs are computed monthly, the actual surface mass-balance is computed yearly and all snow that is accumulated in one year transitions to ice the next year. This invokes the assumption that once surface mass balance is positive in the yearly cycle (on a monthly mean basis), refreezing won't be significant until the start of the next melt season. This avoids issues around tracking snow age and snow amounts between consecutive years at the cost of errors that are overwhelmed by input and parametric uncertainties. For those doing detailed firn modelling, a more refined (likely sub-diurnal) approach would be required.

2.7.2 Submarine melt

Though there has been significant progress in submarine melt parameterizations (as compared in Asay-Davis et al., 2017; Favier et al., 2019), a confident and computationally tractable representation for submarine melt remains an ongoing challenge. This is especially so for glacial cycle contexts for which the required ocean temperature fields are unlikely to be available to the requisite accuracy in the foreseeable future.

The recommended sub ice shelf melt (SSM) representation for the GSM is the (-DSSMslope -DSSMslopeLJGW19) buoyant plume model from Lazeroms et al. (2019). It give the SSM (ssm in m/yr)) as a function of the basal ice angle (θ) , ambient ocean temperature near the grounding line (T_a), local ice depth (z_b) and a non-dimensional horizontal coordinate x:

$$
\begin{aligned}
ssm &= C_{\mathrm{SSM}} \cdot FS(\gamma(\theta)) \cdot (T_a - T_{fz})^2 \cdot M_0(x(\gamma(\theta))) \\
FS(\gamma) &= D_s^{1/2} \cdot \left[\frac{C_d^{1/2}\Gamma_{TS} \cdot \gamma}{(C_d^{1/2}\Gamma_{TS} + C_T + \gamma))} \right]^{3/2} \left[\frac{1 - C_{\rho 1} C_d^{1/2}\Gamma_{TS}}{(C_d + \gamma)} \right]^{1/2} \\
M_0(x) &= \frac{1}{2\sqrt{2}} [3(1-x)^{\frac{4}{3}} - 1][1 - (1-x)^{\frac{4}{3}}]^{\frac{1}{2}} \\
x(\gamma) &= \min\left(\lambda_3 \frac{z_b - z_{gl}}{T_a - T_{fz}} \left[1 + C_\epsilon \left(\frac{\gamma}{C_d^{1/2}\Gamma_{TS} + C_T + \gamma} \right)^{\frac{3}{4}} \right]^{-1}, 1.0 \right) \\
\gamma(\theta) &= E_0 \cdot \sin(\theta);\ E_0 = 0.036 : \text{Entrainment coefficient} \\
C_d^{1/2}\Gamma_{TS} &= 5.9 \times 10^{-4} : \text{Effective thermal Stanton number} \\
C_d &= 2.5 \times 10^{-3} : \text{Drag coefficient} \\
C_T &= 1.4 \times 10^{-5}; C_\epsilon = 0.6; C_{\rho 1} = 2.0 \times 10^2 \\
D_s &= \frac{\beta_s S_a g}{\lambda_3 (L_w / c_p)^3};\ \beta_s = 7.86 \times 10^{-4} \mathrm{psu}^{-1};\ S_a = 34.65\,\mathrm{psu};\ \lambda_3 = 7.61 \times 10^{-4} \mathrm{K/m} \qquad (22)
\end{aligned}
$$

The depth of the plume source grounding line (z_{gl}) and associated location and depth for extraction of T_a is determined via a downslope search. The reference freezing temperature (T_{fz}) at the grounding line is depth corrected. There is the option of subjecting T_{fz} to regional or whole grid ice shelf ensemble parameter dependence (CT_{ssmCut}) to partly compensate for limitations in the ocean temperature forcing:

$$T_{fz} = CT_{\mathrm{ssmCut}} - \lambda_3 \cdot z_{gl} - 2.0^o C \qquad (23)$$

https://doi.org/10.5194/gmd-2024-175
Preprint. Discussion started: 17 January 2025

A related limitation is the lack of accounting for horizontal advection due to sub ice shelf ocean circulation. The overall SSM ensemble parameter C_{SSM} adds further parametric degrees of freedom to partly compensate for these error sources.

There are two options for subshelf melt at grounding line grid cells. In accordance with resolution convergence tests of different submarine melt treatments for grounding line grid cells (Seroussi and Morlighem, 2018), the default (no special compile flag) option is that the GSM only applies the above subshelf melt parameterization to fully floating grid cells. However Seroussi and Morlighem (2018) only tested subshelf melt parameterizations that do not decrease in magnitude near the grounding line (before application of subgrid relative floating area scaling), unlike that of the recommended Lazeroms et al. (2019) plume parameterization. Furthermore, the experiments only evaluated a 100 year retreat scenario and it remains unclear whether their conclusions hold in the case of a glacial advance and subsequent retreat scenario of more relevance for glacial cycle modelling. As such, the GSM has an option for scaling of subshelf melt by the relative subgrid area that has floating ice (-DGLssm, similar to configuration SEM1 in Seroussi and Morlighem, 2018). This has an added scaling parameter (RfactGLssm) to further reduce grounding line grid cell subshelf melt. Sensitivity tests have found grounding retreat and advance to be more stable for RfactGLssm$=0.5$ compared to the simulations with subshelf melt only for fully floating grid cells.

Calving face submarine melt is taken from the results of high resolution Massachusetts Institute of Technology general circulation ocean modelling (Rignot et al., 2016). We use their extracted analytical fit for submarine melt of west Greenland outlet glaciers. This has a dependence on the approximated meltwater velocity (q, m/day) and the interpolated (or extrapolated) ocean temperature ($T(x,y,z)$). In detail, the submarine face melt (q_m in m/day) at depth d is given by:

$$q_m(d) = (A \cdot d \cdot q^a + B \cdot C_{\mathrm{face}}) \cdot \max(T_F(x,y) - CT_{\mathrm{ssmCut}}\ ,\ 0)^{\beta} \tag{24}$$

with $a = 0.39$, $A = 3 \times 10^{-4}$ m/day, and $\beta = 1.18$ as per Rignot et al. (2016). The freezing point (CT_{ssmCut}) is treated as a ensemble parameter to impose bias corrections for the ocean temperature forcing. $B = 0.15 \cdot 180$ as per Rignot et al. (2016) assuming an average of 180 melt days and has added ensemble parameter scaling (C_{face}). The above equation is rescaled for m/yr quantities and q is approximated by scaling the sum of the subglacial melt rate and surface runoff by the grid cell area to marine face area ratio.

2.7.3 Marine ice shelf calving

For marine floating ice calving, two dynamical controls are assumed. First, a stress-balance crevasse propagation parameterization following Pollard et al. (2015) is used. This is expressed as a horizontal wastage rate (W_c) (though numerically applied as an appropriately scaled contribution to the surface mass-balance forcing) subject to ensemble parameter C_{calv}:

$$W_c \;=\; C_{\mathrm{calv}} \cdot 10\,\mathrm{km/yr} \cdot \max[0, \min[1, (r - r_c)/(1 - r_c)]]\ , \tag{25}$$

$$r \;=\; (d_s + d_b + d_a + d_t + d_w)/H_t\ ;\ r_c = 0.75 \tag{26}$$

where each $d_?$ term represents a contribution to crack depth propagation. As calving in the GSM is only allowed for ice marginal grid cells, the sum of the contributions from strain rate divergence to dry-surface (d_s) and basal (d_b) crevasses is

https://doi.org/10.5194/gmd-2024-175
Preprint. Discussion started: 17 January 2025

given by that for a free floating unconfined ice face (*e.g.,* Schoof, 2007):

$$d_s + d_b = H_t/2 \tag{27}$$

Following Pollard et al. (2015), an accumulated strain contribution is included to crudely account for upstream accumulation of fine-scale fracturing from strain divergence:

$$d_a = H_t \; \max\left[0, \ln(u/800)\right]/ln(1.2) \tag{28}$$

To improve GSM fits to present day (PD) observed Antarctic ice shelf extents, the 1600 m/yr value for the denominator in Pollard et al. (2015) was reduced by a factor of 2.

The d_t term is added to prevent floating ice thinner than ~ 150 m in accord with present-day Antarctic ice shelves. Our implementation has slight alterations to that imposed in Pollard et al. (2015) to better facilitate ice margin expansion. These are the use of the maximum of adjacent grid cell ice thickness (H_{adjmx}) instead of the marginal ice thickness (H_t) and an increase of the saturation threshold to 200 m from 150 m:

$$d_t = \begin{cases} H_t \; \max(\,0.,\, \min(\,1,\, (200 - H_{\text{adjmx}})/50)) & \text{Depth}_{\text{ocean}} > 300\,m, \\ 0 & \text{else} \end{cases} \tag{29}$$

Recovery of present-day AIS ice shelf extent is also further improved with imposition of a minimum marine depth of 300 m for activation of this component.

The remaining d_w term in eq. 26 is the additional surface crevasse depth due to hydrofracturing from water infill:

$$d_w = C_{\text{hydCrk}} \cdot 100 \cdot (\text{GSM surface runoff flux (m/yr)})^2 \tag{30}$$

This matches the corresponding term in Pollard et al. (2015) for $C_{\text{hydCrk}} = 1$ as motivated in that paper.

The default terminal ice thickness (H_t) estimate in the GSM is simply $\max(0.95\,H, 200\,m)$ with the floor value set in line with what is mostly observed for the margins of large Antarctic ice shelves. The code includes (as a compile flag - DhedgeActive) the downstream thinning option of Pollard et al. (2015). The activation of this option tends to increase numerical instability with otherwise limited impact on results after accounting for compensation from ensemble parameter variations.

Unlike many other ice sheet models, a second control is the assumption that if summer sea surface temperature forcing (approximated by 2 m air temperature) is too cold to permit sea-ice free conditions (summer T_{2m} <TcalvCut=-2^oC), then iceberg production will cease due to back-stress and potentially reduced adjacent marine convection (driving undercutting). This is motivated by both the tendency for seasonal calving in the high Canadian Arctic to initially occur after the loss of land-fast sea ice and the bracketing of the Antarctic ice shelf margin with the -2^oC and -6^oC mean summer sea surface isotherms. The one exception is that complete calving is assumed for ice shelves beyond the continental shelf break. This shelf break location is set by present-day depth equal to GSM parameter rDepthDeepCalv(Ice sheet Index)= 860 m, except for Antarctica where a 1700 m depth was found necessary to permit present-day fringing ice shelf margins around the Antarctic Peninsula

https://doi.org/10.5194/gmd-2024-175
Preprint. Discussion started: 17 January 2025

Geoscientific Model Development
Discussions
Open Access

as observed. This deep sea calving reduces computational cost where an ice shelf would definitely have no confinement and therefore impose no backstress upstream.

Ice calving is computed for each marine ice margin grid cell interface, even if this entails more than one interface of a grid cell. Given the limited grid resolution, an ice covered grid cell is taken as marine margin if it has an adjacent grid cell with ocean depth greater than 40 m and ice cover less than 5 m thick. The GSM tracks open marine basin connectivity to the ocean and shuts down calving when the connectivity is lost on the assumption that iceberg congestion will adequately increase backstress on the calving front to terminate calving.

2.7.4 Tidewater calving

We use the identical tidewater calving scheme of Pollard et al. (2015), with the horizontal calving rate (W_{ct} in m/yr) computed as:

$$W_{ct} = C_{\text{calv}} \cdot \; 10\,\text{km/yr} \cdot \; \max[0., \min[1, (h_{\text{sw}}\, F - H_c)/10]] \tag{31}$$

where

$$F = \frac{\theta}{\max[10^{-6}, 2(1 - \theta/2 - d_w/H_{\text{GL}})]} \tag{32}$$

and the critical ice thickness for cliff failure is set to $H_c = 100\,m$. H_{GL} is ice thickness at the grounding line (computed from applying the flotation condition to the horizontally interpolated grounding line depth). $h_{\text{sw}} =$ is height above water at grounding line, and the contribution from crevasse water depth (d_w) is computed as above for ice shelf calving. θ is related to the back stress on an ice shelf with value 1 for an unbuttressed ice shelf or no floating ice at all. As we restrict calving to the ice marginal grid-cell, the model has a default option of permanently setting θ to this value.

2.7.5 Lake calving

As lake margins of ice sheets are indicative of relatively warm conditions, the GSM lacustrine calving model assumes that surface melt filling of cracks and associated crack propagation is not a control on lake calving. Instead, it is assumed that the main control is the available heat to melt icebergs. Once all excess heat is used up, the lake is assumed to quickly choke up with icebergs, and thereby block further calving.

Given the large process uncertainties, the potential iceberg melt is just set to the total computed net potential surface melt of adjacent lake filled grid cells times a GSM parameter (flac). This thereby lacks accounting for extra lake grid cells that are not in contact with the ice-sheet. It also assumes that the effective surface albedo of the lake will be dominated by that of icebergs and bergy bits and thus the melt potential for a unit area is close to that computed (the surface melt calculation doesn't have a separate albedo for lake cover).

Two further somewhat adhoc conditions are imposed to ensure there is sufficient exposure of the grid cell ice to adjacent cell water and sufficient lake depth to enable heat circulation. These requirements are : 1) local water depth of calving grid cell is

https://doi.org/10.5194/gmd-2024-175
Preprint. Discussion started: 17 January 2025

Geoscientific Model Development
Discussions

more than the lesser of SLACMX (set to 50 m) and the local ice thickness, and 2) ice-free adjacent cell water depth is greater than SLACMIN (set to 20 m except for EA = 33 m to enable adequate EA ice sheet expansion in certain regions).

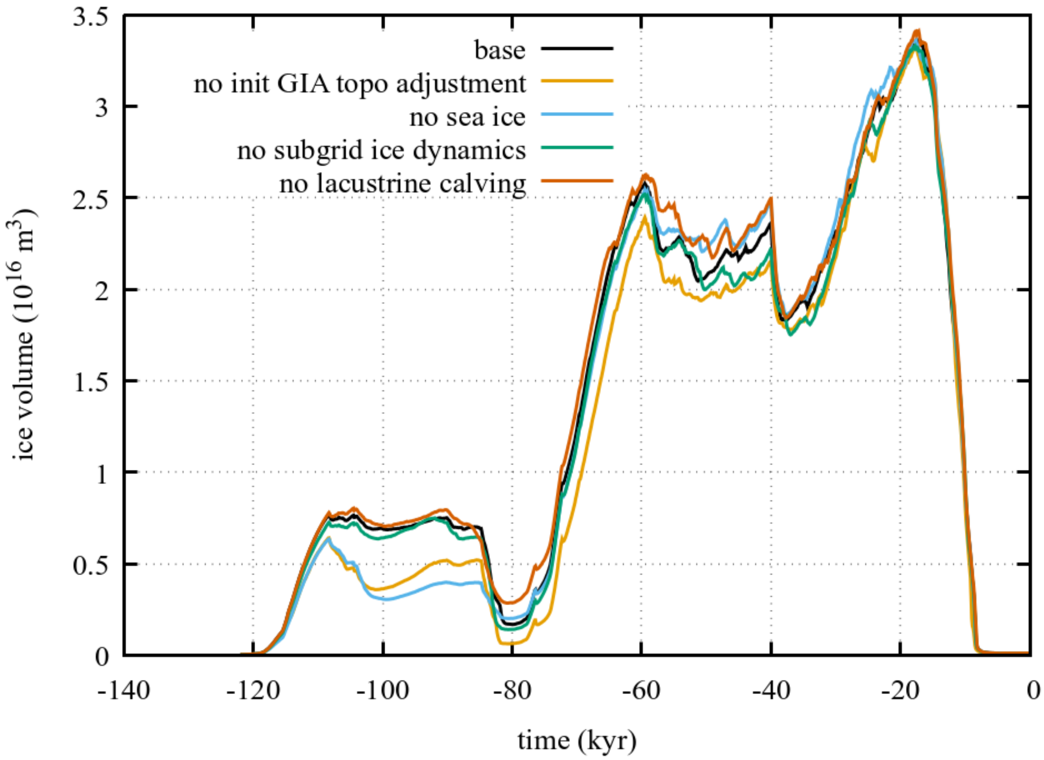

Figure 3. Some example GSM sensitivities to one at a time process removal for a NAIS simulation.

For an example North American ice sheet (NAIS) simulation, inhibition of lacustrine calving (cf Fig. 3) has a significant impact on ice sheet volume during the 80 ka interstadial and 60 ka to 40 ka glacial interval.

2.8 surface drainage solver

The solver simply routes water downslope, filling depressions (lakes), until a marine depth of 200 m or until no water is left. It computes marine drainage summaries for defined drainage basins, for total (including precipitation over ice-free land), ice sourced, and solid-fraction only drainage. The solver uses a modified version of the USGS EROS HYDRO1k hydrologically self-consistent DEM (USGS, 2004). The drainage preserving upscaling of the DEM includes some by hand corrections to capture the controlling sill elevation for the southern drainage of the central LIS (*e.g.,* pro-glacial lake Agassiz). Details on the solver, drainage topography creation, and validation are in Tarasov and Peltier (2006).

https://doi.org/10.5194/gmd-2024-175
Preprint. Discussion started: 17 January 2025

Geoscientific Model Development Discussions

The algorithm is run every dlong years (default is 100 year) and accumulates mean surface runoff and marine ice discharge over the dlong interval. A discharge map is also created for coupling with climate models or other such contexts.

Given the limited subaerial Greenland and Antarctic terrestrial surfaces over which grid-cell scale pro-glacial lakes could form, the surface drainage solver is generally not activated for these ice sheets.

2.9 Sea and lake ice formation

The GSM includes a simple thermodynamic sea and lake ice formation module. The inclusion of the former is motivated by evidence for paleocrystic ice (floating ice grown directly from local precipitation and not terrestrially sourced, Bradley and England, 2008). It was also found necessary to remove spurious ice holes in the Barents and Kara Seas that occasionally developed under glacial moisture starved conditions. As shown in Fig. 3, sea ice inclusion can play a significant role in increasing NAIS glacial inception ice volume, a long standing challenge for paleo ice sheet models when coupled to full climate models.

The lake and sea ice basal accumulation model assumes a monthly approximately thermodynamic steady state for the floating ice, and thereby a linear temperature profile. After a trivial integration this gives growth in effective sea or lake ice thickness (H_f) over time Δt as:

$$H_f(t+\Delta t) = \sqrt{H_f(t)^2 + \Delta T(t)\cdot \Delta t \cdot k/(\rho_i \cdot L_w)} \tag{33}$$

where L_w is the latent heat of fusion for water, k is the thermal conductivity of ice, and

$$\Delta T(t) = \max(0, -3^oC - T_{2m}(t)) \tag{34}$$

The change is ice thickness is not directly imposed in the GSM but instead converted to an effective contribution to the surface mass-balance term (otherwise this ice accumulation would break mass conservation in the surface runoff discharge calculation). This ice remains subject to all the other mass-balance processes in the GSM.

2.10 Climate forcing

The GSM climate forcing generates evolving monthly precipitation, near surface air temperature, and ocean temperature fields. It includes dependence on various glacial indices as detailed below.

2.10.1 glacial indices for climate forcing

The GSM has various glacial indices for driving components of the climate forcing. A to date unique feature is the addition of monthly dependence for the glacial indices. The traditional reliance on mean annual glacial indices (*e.g.,* Marshall et al., 2000; Scherrenberg et al., 2023) hides the significant impact of changes in seasonality over the glacial cycle. For example August – February differences range up to 25% over the last glacial cycle for the EBM derived glacial index. For a more advanced coupled ice-climate model over the last two glacial cycles, the glacial index differences can exceed 100% (Geng et al, manuscript in preparation).

https://doi.org/10.5194/gmd-2024-175
Preprint. Discussion started: 17 January 2025

Geoscientific Model Development
Discussions
Open Access

I_e is the mean monthly EBM temperature anomaly relative to present-day over the 40N:80N latitudinal band divided by corresponding LGM anomaly. The I_g index uses ensemble parameter rWtEBMindx to weigh I_e with an input glacial index chronology specified in the runscript. The latter glacial index can be in mean annual format from a deep ice core isotopic record. There is also a compile flag option to include a monthly glacial index input from a more advanced coupled ice and climate model.

For computing 2 meter air temperature, I_g is subject to two ensemble parameters, C_{IT} and Θ_T, respectively adjusting amplitude and phase:

$$I_c = \mathrm{SIGN}(C_{\mathrm{IT}}, I_g) \cdot |I_g|^{\Theta_T} \tag{35}$$

For controlling the Atlantic meridional overturning circulation impact parameterization (cf next subsection), the annual I_N index uses the average of the scaled pCO2 forcing $(\min(280, pCO2(t))/90)$ and a North Atlantic index for the scaled mean annual EBM temperature anomaly over 40^o to 20^o W and 40^o to 45^o N region. I_N ranges from about -5 to 0.

The I_d ice dome index is a function of the maximum elevation of the main ice dome (h_{Idmx}). It is subject to ensemble parameter h_{Ides} as following

$$I_d = \min((\max(h_{\mathrm{I_{dmx}}} - 1\,\mathrm{km}), 0)/(2\,\mathrm{km}), 1)^{(2-1.5\,h_{\mathrm{Ides}})} \tag{36}$$

The index is used to partly account for possible large scale circulation response to the changing elevation of the main ice dome as discussed below.

2.10.2 surface climate forcing

The biggest source of uncertainty for glacial cycle ice sheet modelling is the climate forcing. To partly address this, the GSM features different climate forcing options that can be combined under ensemble parameter specified weighting.

First of all, it includes an asynchronously coupled 2D energy balance climate model (EBM), running at spherical harmonic truncation T11 with non-linear sea ice and snow albedo feedbacks (Deblonde et al., 1992).

Sea level temperature (T) is computed by an approximation for the energy balance of the tropospheric and mixed-layer ocean column that only accounts for vertical radiative fluxes, horizontal diffusive heat transport, and a parameterized North Atlantic oceanic heat flux contribution (NAHF):

$$\begin{aligned} C(\mathbf{r})\frac{\partial T}{\partial t} &= (S_o a(\mathbf{r},t) S(\theta,t)/4 + \mathrm{NAHF}(\mathbf{r},t)) + \Delta Rad_{CO2} + \Delta Rad_{CH4} + \Delta Rad_{\mathrm{otherIce}} \\ &\quad - (A + B(T(\mathbf{r},t) - \lambda_{\mathrm{ebm}} h(\mathbf{r},t)) - \nabla_h [D(\theta)\nabla_h T(\mathbf{r},t)]) \end{aligned} \tag{37}$$

The equation is solved for monthly mean equilibrium solutions on default 100 year increments. The linearized long-wave emission $(A + B(T(\mathbf{r},t) - \lambda_{\mathrm{ebm}} h(\mathbf{r},t)))$ accounts for reduced emission at higher elevations due to cooler temperatures and is implemented via a constant lapse rate (λ_{ebm}). The absorbed short-wave radiation is set to the product of the solar constant S_o ($1360\ \mathrm{W\,m^{-2}}$), an effective coalbedo $a(\mathbf{r},t)$, and the solar distribution function $S/4$. The coalbedo has latitudinal dependence derived from satellite observations (Stephens et al., 1981) and seasonal dependence on snow and sea ice cover. The time-dependent orbital parameters for S are computed as per Berger and Loutre (1991). The heat capacity C has four possible values

Geoscientific Model Development Discussions

according to surface type (land, land ice, sea ice, and water). The diffusion coefficient D is tuned to preserve the present-day observed mean latitudinal temperature gradient. The radiative forcing due to changing atmospheric greenhouse gas (GHG) concentrations (currently restricted to CO2 and CH4) is accounted as per Myhre et al. (1998) (though with rounding up of the numerical coefficients to partly compensate for missing feedbacks in the EBM):

$$\Delta Rad_{CO2} = 6 \ln\left(\frac{pCO2}{300\, ppmv}\right) \tag{38}$$

for CO2 and

$$\Delta Rad_{CH4} = 0.04\,(\sqrt{pCH4} - \sqrt{1100\, ppbv}) \tag{39}$$

for methane. The chosen reference concentration values are between those corresponding to pre-industrial and a 1980:2000 CE reference climate interval. This is to account for far from complete transient response to present-day GHG changes.

Given the impact of heat transport by the Atlantic meridional overturning circulation and its changes over the past, as well as to improve fits to present-day observed climate, the EBM has an added horizontal surface ocean heat flux ($\mathrm{NAHF}(\mathbf{r},t)$). This flux has geographically dispersed weak sinks, and a source concentrated around (17.5^o E, 67.5^o N), with the central position determined by root mean squared error minimization against present-day reanalysis climatology. This represents a displacement by about 15 degrees east from the climatologically observed net ocean surface to air heat fluxes, presumably accounting for eastward advection by mid-latitude westerlies. The heat flux has various choices of dependencies on the current I_N index value and the state history set by a compile flag. The current recommended choice is -DNAHFv3. It is also a function of pCO2 forcing and sea level, configured so as to induce Dansgaard-Oeschger-like oscillations in air temperature. Given the adhoc nature of the implementation, we leave the documentation to the source code (pGSM.F90) for those interested.

A linear version of the EBM (without seasonal snow/ice albedo feedback) has previously been evaluated against observations and output from an early version of the NCAR CSM general circulation climate model (run at wave number 15 rhomboidal truncation). It was found to capture much of the millennial scale response on this spatial scale especially for the Northern Hemisphere (Hyde et al., 1989). Given that the EBM lacks atmospheric dynamics and as such won't be able to capture the effects thereof, the model is generally run in anomaly mode, with the EBM providing the climate forcing anomaly relative to a present-day monthly climatology (T_{rean}) and subject to an ensemble scaling parameter C_{EBM}:

$$T = C_{\mathrm{EBM}}\,(T_{\mathrm{EBM}}(t) - T_{\mathrm{EBM}}(0)) + T_{\mathrm{rean}} \tag{40}$$

This presumes radiative perturbations dominate the climate system response to orbital forcing changes.

Comparison of PMIP II and III simulations along with a dedicated set of CESM 1.2 experiments (Bakker et al., 2020) has identified Siberia as the region having the highest LGM summer temperature sensitivity to climate model choice and configuration. Lofverstrom and Liakka (2018) have also shown that strong grid resolution dependence for Northern Eurasian June/July/August (JJA) surface temperatures for the NCAR CAM3 atmospheric GCM when run below T85. Given the low T11 resolution of the EBM and its lack of atmospheric dynamics, an added parameterization is used to correct excessive glacial summertime cooling as evidenced by Siberian ice growth in simulations contrary to the geological record. The additive

https://doi.org/10.5194/gmd-2024-175
Preprint. Discussion started: 17 January 2025

Geoscientific Model Development Discussions

correction field is approximately derived from differences between EBM and mean PMIP LGM JJA sea-level temperatures. On the assumption that relevant circulation changes are driven by topographic changes, this warming is scaled by product of the Fennoscandian ice dome elevation index I_d and the GSM ensemble parameter rSumPlusEBM.

When run in single ice sheet mode, the EBM will under predict glacial cooling as a result of the missing radiative impact of ice sheets that are not modelled. As such, the GSM has an option (-DdRadIndx) to implement a scalar decrease in shortwave input to compensate for missing ice sheets. Concretely, this is implemented as

$$\Delta Rad_{\mathrm{otherIce}} = -\mathrm{dradSea} \cdot \max(-\mathrm{scalarSealevel}/125\, m, 0)^{1.5} \tag{41}$$

with parameter dradSea set in the run script (generally ranging from 1 to 7 W/m^2, determined by comparison of EBM results with single and global ice sheet configurations).

The second climate forcing option is a glacial climate index (I_c) weighted addition of a full-glacial (LGM) climatological anomaly (relative to present) to a present-day reanalysis climatology for both mean monthly two meter air temperature and precipitation. The glacial climatology ($T_{\mathrm{PMIP}}(LGM,x,y)$ and $P_{\mathrm{PMIP}}(LGM,x,y)$) is derived from the highest resolution three to four climate model simulations in past PMIP experiments. It is the sum of the mean of the simulations and the top one to three inter-model Empirical Orthogonal Functions (EOFs). The addition of each EOF component for precipitation and two meter air temperature is subject to individual ensemble parameter weighting (fPEOF(n_{Peof}) and fTEOF(n_{Teof})) to account for the significant inter-model differences in the PMIP simulations.

For North America, the orographic forcing from a large Keewatin dome has been shown to significantly perturb atmospheric circulation and therefore North American climate (Kutzbach and Wright Jr, 1985; Andres and Tarasov, 2019). To partly address this dependency on changing dome size over a glacial cycle, the GSM takes advantage of the difference in LGM boundary conditions between PMIP I and PMIP II with the former have no Keewatin ice dome (ICE4G Peltier, 1994) and the latter having an excessively high Keewatin ice dome (ICE5G Peltier, 2004). The Keewatin dome elevation index I_d is used to weight mean LGM PMIP I and PMIP II temperature and precipitation fields.

Greenland has a further temperature component parameterized as functions of latitude, longitude, surface elevation, month, and glacial index, based on those derived from linear regression of present-day climatologies (Fausto et al., 2009). Greenland also includes an added Holocene latitudinal warming gradient (T_{agy}) to capture one of the main regional forcings that had been previously found to help address misfits in ensemble fitting of deglacial Greenland ice sheet simulations to paleo and geophysical constraints (Lecavalier et al., 2014). This strong high latitude warming also has support from analysis of the isotopic record of the Agassiz ice cap (Ellesmere Island, Canada, Lecavalier et al., 2017). The forcing component takes the form:

$$T_{\mathrm{agy}} = C_{\mathrm{HTM}}\, T_{\mathrm{ag}}\, (\max(0.0, \min(1.0, (\theta - 60.0)/\Theta_{\mathrm{wrm}})))^2 \tag{42}$$

with explicit dependence on latitude (θ) and ensemble parameters C_{HTM} and Θ_{wrm}. $T_{\mathrm{ag}} = 9°\mathrm{C}$ for the early Holocene then linearly ramped down to 0 over the 10.15 ka to 4.7 ka interval. As this extra warming is beyond that inferred from GRIP and NGRIP, the forcing is linearly ramped down to 0 over the 0 to 2000 masl surface elevation interval.

A third temperature forcing component option for Antarctica is simply a scalar glacial index forcing plus 10^{o}C forcing per pCO2 doubling and lapse rate vertical temperature adjustment (as in Pollard and DeConto, 2012) applied to the present-day reanalysis climatology.

A major problem with glacial indexed interpolation of input GCM fields is that these fields have a very strong imprint of their ice sheet boundary condition. The implicit migration of the ice sheet margin between GCM time-slices and the impact thereof is unlikely to be captured by the imposed linear interpolation for sea level temperature. As such, an optional parameterization (-DHboostTindx), imposes an increase of the glacial index (limited by the LGM value of 1) whenever the GSM grid cell is ice covered. This is linearly imposed for thin ice as follows:

$$I_c = \min(1\ ,\ I_c + \min(1\ ,\ H(x,y)/500) \cdot I_{\text{H+}}) \tag{43}$$

with $I_{\text{H+}}$ being an ensemble parameter (nominal range 0:0.2). In the future, this may be made more accurate by adding a blurred version of the GCM glacial state ice mask, so that changes are only imposed where there is a discrepancy between the GCM ice mask and the GSM grid cell ice cover. This would also enable the clean addition of local glacial index reduction if the GSM has no ice cover in a grid cell for which the GCM LGM ice mask has ice.

The first precipitation forcing option is relative interpolation between the present-day observed climatology $P(0,x,y)$ (Hersbach et al., 2023) and the LGM field from the PMIP ensemble $P(LGM,x,y)$ using the following function of the glacial index $I_g(t)$:

$$P(t,x,y) = P(0,x,y) \cdot \left(\frac{C_{\text{pre}} \cdot P_{\text{PMIP}}(LGM,x,y)}{P_{\text{PMIP}}(0,x,y)} \right)^{I_g(t)^{\Theta_P}} . \tag{44}$$

We introduce the “ensemble phase factor” (Θ_P) to parameterize some of the uncertainty associated with the transition from interglacial to glacial atmospheric states. C_{pre} is a global ensemble scale parameter.

The second precipitation forcing option is a generalization of the Clausius-Clapeyron relation for the saturation vapour pressure dependency on temperature. This precipitation component (P_T) is also subject to ensemble parameter C_{Tp} as followings:

$$P_T = \exp(C_{\text{Tp}} \cdot (T_{2m} - T_{2m0}))P_0 \tag{45}$$

where the 0 subscripted components are from present-day reanalysis.

Precipitation is further controlled by a range of regional parameters. Most take the form of a desert-elevation (Budd and Smith, 1981) threshold control over a specified geographic region. Ensemble parameters set the regional threshold in an array (rdes, listed as “desert-elevation cutoffs” in Table 3). Computed precipitation is then subject to the factor:

$$\exp(C_{\text{des}} \cdot \max(h_{\text{dk}} - (I_{\text{dk}} \cdot \text{rdes}(x,y) + (1. - I_{\text{dk}}) \cdot h_{\text{des0}} + \text{fmindeselcut}), 0)) \tag{46}$$

where h_{dk} is 75% of the difference in elevation in kms between the GSM and the I_{dk} index interpolated orography for the climate model fields. The I_{dk} index is given by the average of the climate index (I_c) and dome elevation index I_d (cf section

2.10.1) to crudely insert global and regional scale dependencies of atmospheric circulation. fMINdeselcut has a default value of -0.5 km to allow for potentially excessively high input orographies. These controls are perhaps best interpreted as regional smooth limits on maximum ice elevation facilitating fit to deglacial constraints operating within the large uncertainties for paleo precipitation.

2.10.3 orographic precipitation down-scaling

Paleo ice sheet modellers have traditionally relied on a simple exponential function of surface elevation or temperature to downscale precipitation fields from lower resolution climate model output that poorly resolves the orography. However, though this approximately captures the Clausius-Clapeyron dependence on temperature, it does not account for the orographic forcing of precipitation that can drive higher precipitation at higher elevations and wind-shadowing on leeward sides (*e.g.,* Roe, 2005, for a review). To account for these effects, the GSM uses an orographic down-scaling approach that assumes precipitation corrections for orography on the windward side are proportional to the ratio of mean vertical wind velocities between high resolution and low resolution orographies as diagnosed by the scalar product of the horizontal wind velocities and surface slopes. In detail the windward orographic correction factor (fPorog) is

$$\mathrm{fPorog} = \sum \min(\max((\mathbf{U}_{\mathrm{GCM}} \cdot \mathbf{slope}_{\mathrm{GSM}} + \mu_p)/(\mathbf{U}_{\mathrm{GCM}} \cdot \mathbf{slope}_{\mathrm{GCM}} + \mu_p), \mathrm{FPorogMN}), \mathrm{FPorogMX}) \cdot \mathrm{Uweight} \quad (47)$$

The factor is applied in the downscaling of coarse-gridded input precipitation climatology. The model uses both mean monthly wind velocities as well as standard deviations thereof to account for intra-monthly variability. This involves a summation of mean and mean $\pm 1\sigma$ wind velocities (($\mathbf{U}_{\mathrm{GCM}}$) with appropriate weighting (Uweight). μ_p is an ensemble parameter that regularizes the orographic forcing. For the leeward side, the orographic forcing factor is set to the regularized difference of vertical velocities:

$$\mathrm{fPorog} = \sum \min(\max((\mathbf{U}_{\mathrm{GCM}} \cdot \mathbf{slope}_{\mathrm{GSM}} - \mathbf{U}_{\mathrm{GCM}} \cdot \mathbf{slope}_{\mathrm{GCM}} + \mu_p)/\mu_p, \mathrm{FPorogMN}), \mathrm{FPorogMX}) \cdot \mathrm{Uweight} \quad (48)$$

The above value of fPorog is further scaled for each GSM grid cell to ensure that precipitation is conserved at the input GCM grid cell scale. As such, the latter is kept purposely coarse (on the order 8 by 4 degrees in longitude and latitude respectively). An analysis of the strong impact of this downscaling approach for fully coupled GSM and climate model simulations is given in Bahadory and Tarasov (2018). This orographic correction is only applied to the components of the precipitation from climate model output.

2.10.4 ocean climate forcing

Ocean temperature forcing is required for both marine calving and submarine melt. For the former, ocean surface temperature is set to the mean sea level summer temperature from the atmospheric forcing with the condition that ocean surface temperature cannot go below the freezing point ($-2^{\circ}\mathrm{C}$). For the latter, either the ocean basal (default) or the average water column (-DToceanDepthAvg) temperature from a low resolution input chronology is horizontally interpolated. For our source chronology, we use the ocean temperature field from the Transient Climate Evolution (TRACE Liu et al., 2009) deglacial simulation

https://doi.org/10.5194/gmd-2024-175
Preprint. Discussion started: 17 January 2025

carried out with the CESM Earth system model for which only mean decadal annual average ocean temperature fields were available. The chronology is time interpolated for the last deglacial interval covered by the simulation and otherwise computed by glacial index (with index I_g) weighted interpolation between the full glacial (LGM) and present-day time slices for any other time. To partly address uncertainties in the relationship between the glacial index and the ocean state, the index is subject to an ensemble parameter exponential phase factor (Θ_{To}). As such, the applied glacial index is $I_g^{\Theta_{To}}$.

Given the present-day discrepancies in the TRACE fields, we impose a correction for present-day bias using the ECCO ocean state estimate (Fukumori et al., 2018). This bias correction is subject to an ocean state dependent weighting given by ensemble parameter rToceanBiasCor. The latter specifies the bias correction for glacial index value 1 (LGM). The weighting increases to full bias correction at 0 ka. The factor for the added present-day ocean bias correction is rToceanBiasCor + rw (1.−rToceanBiasCor), with rw given by the square root of the fractional time from LGM to present-day of the TRACE time slice. As the ECCO dataset provides monthly means, we use the average of summer and mean annual ECCO ocean temperatures to partly capture summer season warmth, while retaining some partial consistency with the mean annual temperature fields from TRACE.

After an initial set of history matching waves (Tarasov and Goldstein, 2023; Lecavalier and Tarasov, 2024), it was found that the simulated Antarctic contribution to the Eemian high-stand was inadequate. As the largest component of relevant climate forcing uncertainty is the subshelf ocean temperature, this inadequacy was assigned to this uncertainty. As such, the GSM has an option (-DoceanFwarm) to include a glacial index enhancement when warmer then 0 ka ($I_g < 0$). This is subject to ensemble parameter rToceanWrm.

For Antarctica, an imposed controlling sill depth of 500 m for the Ronne-Filchner sector limits the depth from which the ocean temperature is taken even if the grid-cell floating ice depth is below this.

If the model is fully coupled to an Earth systems model, the GSM can use the ocean temperature field from the ocean model. As detailed in Bahadory and Tarasov (2018), to minimize regridding overhead for complicated ocean model grids, the GSM has a default option of just taking ocean temperature profile chronologies for a number of index sites. The chronologies are then applied to specified downstream sectors of the ocean.

2.11 subgrid ice flow and surface mass balance

The subgrid ice flow and surface mass balance component (inclusion via -DSGhyps and make paleonSG) reduces the subgrid topography for each GSM grid cell with thin or no ice cover to a set of hypsometric curves upon which a fast 1D SIA ice flow and sliding calculation is carried out. Surface mass balance for each hypsometric curve uses the same solver as for the full GSM grid. A unique feature is that module accounts for subgrid ice flow between adjacent full grid cells. Details on the module design, impact, and validation are in Le Morzadec et al. (2015).

https://doi.org/10.5194/gmd-2024-175
Preprint. Discussion started: 17 January 2025

Geoscientific Model Development
Discussions

2.12 Ice margin nudging

The GSM has an option of automatically adjusting the surface mass-balance and calving to favourably nudge the computed ice margin when outside of time interpolated input maximum and minimum isochrones. The number of such grid-cell adjustments is summed for each time step as a cost function that can be used for model calibration contexts.

The input nudging chronology is a sequence of time slice raster maps on the GSM grid, with value 0 for regions that are definitely ice free, 1 for regions that are likely ice free or ablation zones, 2 for the likely ice margin location, 3 for accumulation zones, and 4 for regions that likely had thick ice well inside of the accumulation zone. With time interpolation between time-slices, these maps provide a nudging field $I_m(x,y,t)$. The nudging is subject to three ensemble parameters (F_m, F_a, F_c, cf Table 2) that specify onset thresholds as well as strength of nudging. Nudging perturbations to the calculated surface mass balance (SMB) are imposed as follows:

$$\mathrm{SMB} = \begin{cases} \min(0.\,, \mathrm{SMB} - \mathrm{fmgm}\cdot(2\,F_m - I_m)) & I_m < 2\,F_m \,\wedge\, H > 0. \\ \text{accumulation} & I_m > 4 - 2\,F_a \,\wedge\, \text{grounded} \,\wedge\, \max(H_{adj}) > \mathrm{HmgMx} \,\wedge\, V_b < 100 \text{ m/yr} \\ F_c \cdot \mathrm{SMB} & I_m > 4 - 2\,F_a \,\wedge\, \text{floating} \,\wedge\, \text{active calving with effective SMB} < -5 \text{ m/yr} \end{cases} \tag{49}$$

where HmgMx$= 300$ m. The nudging ablation factor fmgm can be either specified directly in the run script (typically ≤ 10 m/yr) or more physically specified (compile flag -DnudgMelt) as the product of a constant (typically 2) and the computed gross surface melt. The condition on maximum adjacent ice thickness ($\max(H_{adj}) > \mathrm{HmgMx}$) for accumulation nudging is imposed to avoid the occurrence of "pancake ice" when extended regions in the nudging chronology switch from eg neutral zone value 2 to accumulation zone 4. The condition on the magnitude of the basal velocity ($V_b < 100$) inhibits accumulation nudging for active ice streams for which the associated lower surface elevations may physically allow some surface melt.

2.13 Subglacial hydrology

As fully detailed and tested in Drew and Tarasov (2023), the GSM has various options for subglacial hydrology. It includes both linked cavity and poro-elastic options for distributed drainage as well as a diagnostic down-pressure-gradient subglacial tunnel solver that thereby avoids CFL constraints which would be prohibitive for glacial cycle modelling.

The GSM also has a much computationally cheaper local 0D hydrology option (enabled with -DNeff0) with a constant drainage rate (given by ensemble parameter rBedDrainRate) leaky bed, and with effective basal pressure (N_{eff}) a non-linear function of basal water thickness as per the poro-elastic version:

$$N_{\mathrm{eff}} = g\rho_{\mathrm{ice}} H \cdot \left(1 - \min\left[\frac{h_{\mathrm{wb}}}{h_{\mathrm{wbCrit}}},\, 1.0\right]^{3.5}\right), \tag{50}$$

where $g = 9.81\,\mathrm{m\,s^{-2}}$ is the acceleration due to gravity, $\rho_{\mathrm{ice}} = 910\,\mathrm{kg\,m^{-3}}$ the ice density, H the ice thickness, h_{wb} the basal water thickness, and h_{wbCrit} an ensemble parameter for effective bed roughness scale (cf Drew and Tarasov, 2023, for motivation and validation).

https://doi.org/10.5194/gmd-2024-175
Preprint. Discussion started: 17 January 2025

Though lacking explicit englacial hydrology, the GSM has a compile flag option (-DZWALLY) to impose local grid cell surface runoff penetration (via assumed moulins) into the local subglacial hydrology system. This assumes that ice is thin enough and crevassed enough for all regions with significant surface runoff to have such englacial hydrological connectivity to the base.

2.14 Subglacial sediment production, transport, and deposition

The optional fully coupled subglacial sediment model includes two choices for erosion process representation, along with subglacial and englacial transport and deposition. It requires basal water pressure from an activated basal hydrology component. The sediment model is described and validated in Drew and Tarasov (2024) building on the early version of Melanson et al. (2013).

2.15 GIA and sea level

Isostatic adjustment of the bed in response to changes in surface load is computed as per a linear visco-elastic field theory for a spherically symmetric Maxwell model of the Earth (Peltier, 1974, 1976). The bedrock displacement $R(\theta,\psi,t)$ is given by a space-time convolution of the surface load per unit area $L(\theta,\Psi,t)$ with a radial displacement Greens function $\Gamma(\gamma,t-t^{'})$ (Peltier, 1974):

$$R(\theta,\psi,t) = \int_{-\infty}^{t} \int\int_{\Omega} L(\theta^{'},\psi^{'},t^{'})\Gamma(\gamma,t-t^{'})d\Omega^{'}dt^{'} \tag{51}$$

Here γ is the angular separation between a source point and field point. The integral is evaluated pseudo-spectrally as per (Mitrovica and Peltier, 1991) with triangular truncation at degree and order 256 or 512.

Bed response is computed every dlong years (default is 100 years). It accounts for all direct changes in surface load, including ice, lake water, and seawater within the ice sheet grid. The GIA calculation requires global surface load change inputs. Therefore, outside of regions covered by the simulation, surface ice load changes follow an input global chronology (currently GLAC2A) for the last glacial cycle and a sea level weighted interpolation between input PD and LGM states for prior time intervals. Not accounting for global ice load changes in Greenland simulations (as is typical for paleo ice sheet modelling) can have significant impacts (cf Figs. 4 and 5).

Surface load and elevation changes due to subglacial erosion and sediment transport can also be turned on with the -DdynSed compile flag (for details, c.f. Drew and Tarasov, 2024).

The load history must be stored as spherical harmonic coefficients and thereby represents a major memory load. In the GSM, only the last 30 kyr of load history are retained, a choice justified by sensitivity tests.

The GSM includes a small archive of Earth model Greens functions (in the form of Love number sets) nominally specified by 3 ensemble parameters for the lithospheric thickness and upper and lower mantle viscosities. The Earth model Love numbers were computed using the mixed collocation method as per Mitrovica and Peltier (1992). The radial elastic structure for this set is that of the PREM model (Dziewonski and Anderson, 1981).

https://doi.org/10.5194/gmd-2024-175
Preprint. Discussion started: 17 January 2025

Geoscientific Model Development
Discussions

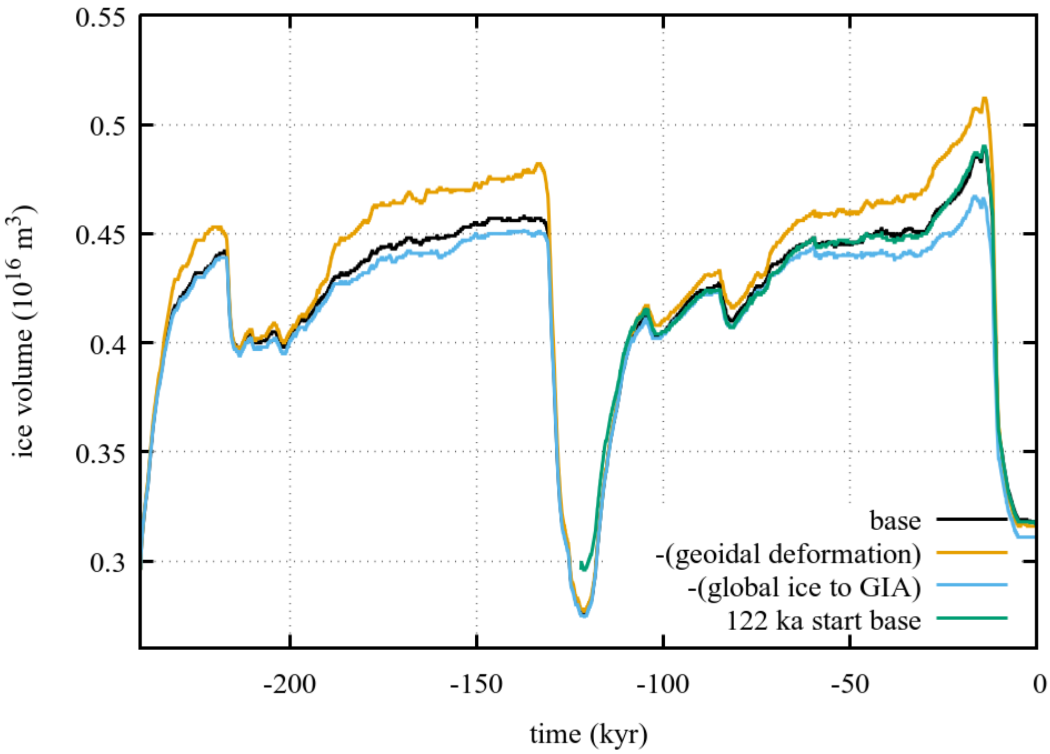

Figure 4. Example process removal sensitivities as given by mean response for a 10 member GRIS ensemble. The listed time series are identified by the GSM process that has been removed.

780 For ice sheets with little or no present-day ice, the GSM has an option to add a GIA correction to the input present-day topography (h_{bo}) for run initialization to partially correct for discrepancies between h_{bo} and the resultant 0 ka topography from a transient simulation due to present-day isostatic disequilibrium. The corrected initial bed topography (h_{boc}) is implemented as

$$h^n_{\mathrm{boc}} = (1+n)\cdot h_{\mathrm{bo}} - \sum_{i=1}^{i=n} h^i_{\mathrm{bf}} \tag{52}$$

785 where n is the number of iterated full glacial cycle simulations applied to create the present-day discrepancy correction, h^n_{bf} is the 0 ka final bed topography from a transient simulation using the previous iteration of the corrected initial topography h^{n-1}_{boc}. This approach can be justified inductively, starting from $h^1_{\mathrm{boc}} = h_{\mathrm{bo}} + (h_{\mathrm{bo}} - h^1_{\mathrm{bof}})$. To improve generalizability, the corrections are implemented as the average of two different not-ruled-out-yet simulations from previous history matching iterations (for an introduction to history matching, cf Tarasov and Goldstein, 2023). These correction fields need to be regenerated for
790 different Earth models (at least for those that give more than 2 kyr relaxation times). Depending on the Earth viscosity, one

https://doi.org/10.5194/gmd-2024-175
Preprint. Discussion started: 17 January 2025

Geoscientific Model Development
Discussions

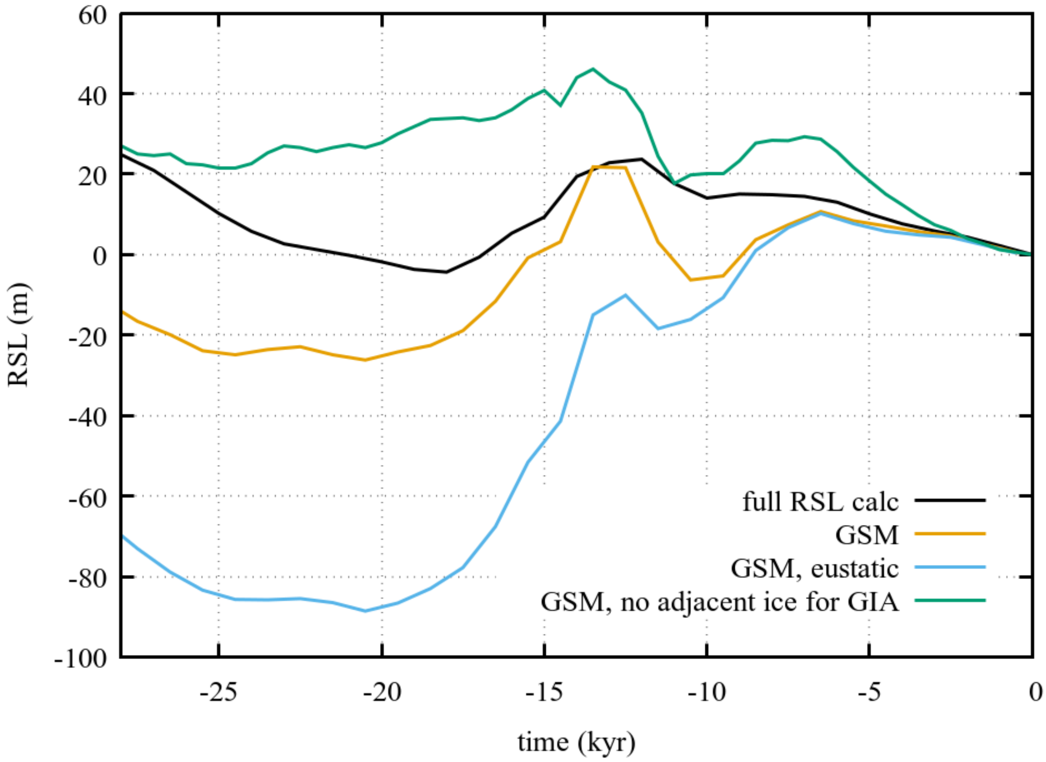

Figure 5. Comparison of computed RSL for Franz Joseph Fjord Greenland (27.42^o west, 73.02^o N). Shown are: the gravitationally-self consistent solution from post-processing ("full RSL calc"), the GSM internal solution using linear geoidal deflection ("GSM"), the solution when geoidal deflection is typically neglected ("GSM, eustatic"), and the GSM solution when ice outside of the regional grid is not accounted for in the visco-elastic bedrock response calculation ("GSM, no adjacent ice for GIA").

to two iterations are generally adequate in that improvements in further iterations are swamped by the impact of varying ice load histories in the subsequent simulations using these corrections fields. This correction to Eemian topography can have a significant impact on simulated NAIS evolution (cf Fig. 3).

For ice sheets with extensive present-day ice cover, the sensitivity of the correction to discrepancies in simulated 0 ka ice thickness (compared to that observed) are too strong for such a correction approach.

Geoidal deflection within the GSM ice sheet grid is computed using a linear approximation. The model modifies the mean volumetric (eustatic) sea level change with a deflection computed as linear contributions from each of the 4 major ice sheets. For ice sheets not modelled, default chronologies for the deflection contributions are read in (currently based on gravitationally-self-consistent post-processing of interim GLAC3 ice sheet chronologies). For the actively modelled ice sheet (referenced by ice sheet index k_i), the deflection (G_d) is simply a relative volume anomaly scaling of the reference input time-interpolated

https://doi.org/10.5194/gmd-2024-175
Preprint. Discussion started: 17 January 2025

Geoscientific Model Development Discussions

deflection ($G_{dInterp}(x,y,t,k_i,k_s)$) contribution from each major ice sheet (referenced by ice sheet index k_s):

$$G_d(x,y,t,k_i) = \sum_{k_s}[\, G_{dInterp}(x,y,t,k_i,k_s)\cdot(\mu_G + \max(vol(t,k_s) - vol_{Ref}(0ka,k_s)\ ,\ 0.))/ \\ (\mu_G + \max(vol_{Ref}(t,k_s) - vol_{Ref}(0ka,k_s)\ ,\ 0.))\,] \qquad (53)$$

where μ_G is a small regularization parameter (with value dependent on the ice sheet). Prior to the last glacial cycle, the geoidal deflection contribution from each ice sheet is a volume anomaly (relative to input present-day ice volume) weighted interpolation between reference geoidal stadial and interstadial time slices. These reference time slices are chosen by matching reconstructed sea level low and high-stands to that of the last glacial cycle.

The geoidal deflection in the GSM is a 0 order approximation. It is better than the typical purely eustatic assumption as shown in Figs. 4 and 5. However, for comparison to RSL data, post-processing of the simulation output with a gravitationally-self consistent solver is necessary. The upgrade of the GSM to a gravitationally-self consistent coupled solution is technically not a major challenge and will likely be added in a future.

The mean sea level in the GSM can be an input or determined from ice volume changes in the GSM with scalings for missing ice sheets.

The GSM also has a simple local relaxation option for GIA. This is useful for GSM testing as well as for running on non-geographic grids (such as for idealized inter-model comparison experiments).

2.16 Noise injection for internal discrepancy assessment or direct noise sensitivity analysis

The GSM has a compile flag (-DIDassess) for activation of noise injection into various poorly constrained component processes and inputs. This can be used for internal discrepancy assessment (Tarasov and Goldstein, 2023) to quantify associated structural uncertainties of the GSM or for sensitivity experiments directly analyzing unresolved process noise impacts. The noise is generated as a sign preserving square of a uniform sampling (-range:range) to ensure substantial noise density near amplitude bounds while concentrating the distribution around 0. The various processes and inputs subject to noise input are listed in Table 5. The choice of noise distribution and amplitude was based on informed author judgment but should be reconsidered by any user based on context and confidence in relevant inputs.

2.17 GSM input fields

Table 6 provides a brief summary of the input data sets used in the GSM.

2.18 GSM initialization

The appropriate initialization of the temperature field in an ice sheet model is, to date, unsettled (*e.g.,* Goelzer et al., 2018; Seroussi et al., 2019). After extensive testing, the following approach was chosen. The initial ice temperature for the Greenland and Antarctic ice sheets is set to analytical approximations of the respective GRIP and EDC ice core borehole temperature profiles scaled from the applied surface temperature to a basal temperature of -6°C for Greenland and -4°C for Antarctica.

https://doi.org/10.5194/gmd-2024-175
Preprint. Discussion started: 17 January 2025

Table 5. noise insertion with -DIDassess

process	max amplitude	dependency
deep geothermal heat flux boundary condition	$\pm 5\%$	input(x,y)
initial basal temperature for ice thermodynamic spinup	$\pm 1^o$C	input(x,y)
surface insolation	$\pm 5\%$	x,y,t
precipitation	$\pm 20\%$	x,y,t
annual glacial temperature index (Tdiffin)	$\pm 1^o$C	input(t)
monthly glacial index (vTdiffin)	$\pm 10\%$	input(t)
glacial index for pre-LGM phasing of ocean temperature	$\pm 10\%$	t
sea level chronology	$\pm 3\%$	input(t before 6.5ka)
effective pressure for basal drag	$\pm 10\%$	x,y,t
basal roughness map uses for basal drag	$\pm 20\% + \pm 10$m	input(x,y)

The choice of the profile locations is motivated by ice dome centres having the slowest velocities and therefore the longest relaxation times to approach a self-consistent vertical temperature profile. This approximation will become more inaccurate farther away from ice dome centres but this will be compensated by the faster evolution to a more self-consistent vertical temperature profile given the higher ice velocities. Setting the whole ice sheet initial basal temperature below the pressure melting point stabilizes the initial ice dynamical solution. The ice sheet velocities are then computed with an SIA solution, and the ice/bed thermodynamics is brought towards partial thermal equilibration (over 1 and 1.5 kyr intervals for Greenland and Antarctica respectively). This is facilitated by temporarily reducing the bed heat capacity by a factor of 1000. The fully coupled hybrid ice dynamics and thermodynamics is then stepped over the asynchronous coupling time step (dlong years, cf section A2 for general GSM code structure), after which thermal partial-equilibration is advanced with the updated ice velocity field (for respectively 3 and 6 kyr intervals). Reduced spinup time intervals are used for other ice sheets and ice caps.

For a set of not-ruled-out-yet Antarctic and Greenland simulations examined, this spinup approach tends to bring the basal warm-based ice fraction to within half of the glacial cycle maximum value. For Antarctica, this spinup approach works especially well for Eemian cold starts. For at least the example run shown in Fig. 6, the grounded ice volume history for a 122 ka to 0 ka simulation is nearly the same between the cold-started run and a run started with the terminal restart file from a 205 ka to 0 ka prior simulation (using the same parameter vector). The approach is sensitive to the initial climate forcing as is evident is the difference between simulations with 206 and 204 ka cold starts (Fig. 6). The O(100kyr) memory in these results is in accordance with the thermodynamical time scale of the Antarctic ice sheet. Given the order of magnitude larger precipitation for Greenland (which reduces the thermal equilibration time scale), this spinup approach results in minimal ensemble mean differences for post 110 ka ice volumes for cold start simulations starting at 240 ka and 122 ka (Fig. 4).

https://doi.org/10.5194/gmd-2024-175
Preprint. Discussion started: 17 January 2025

Table 6. GSM input data sets. All climate fields are in the form of monthly climatologies.

component	data source
present day mean temperature	reanalysis or RCM output
LGM mean temperature	PMIP I to III ensembles (Braconnot et al., 2007, 2012)
present day mean precipitation	reanalysis or RCM output
LGM mean precipitation	PMIP I to III ensembles
present day mean evaporation	reanalysis or RCM output
LGM mean evaporation	PMIP I to III ensembles
present-day and LGM wind field horizontal components:	
monthly means and standard deviations	PMIP III
orographic surface slopes from precip input source boundary conditions	PMIP III
4D ocean temperature chronology	TRACE (Liu et al., 2009)
present-day ocean temperature field	Antarctica (Boeira Dias et al., 2023) otherwise ECCO (Forget et al., 2015)
climate interpolation	inversions of ice core isotopic records (Barker et al., 2011)
bed and surface topography	user choice
hydrologically corrected bed topography	modified HYDRO1K DEM (USGS, 2004; Tarasov and Peltier, 2006)
bed subgrid standard deviation	user choice
sediment thickness map	(Laske and Masters, 1997)
fractional subgrid sediment cover map for till deformation	derived from sediment map (Laske and Masters, 1997)
	and surficial geology map (Fulton, 1995, for NA)
deep geothermal heat flux map(s)	global map of Davies (2013) and/or regional options
Earth model love numbers for GIA calculation	(Love et al., 2016)
Earth radial elasticity	PREM model (Dziewonski and Anderson, 1981)
eustatic sea level chronology	Fairbanks (1989); Waelbroeck et al. (2002); Lisiecki and Raymo (2005);
	Peltier and Fairbanks (2006); Lambeck et al. (2014)

3 Tests and sensitivities

As the core hybrid SIA/SSA ice dynamics solver is from the PSU3D model (Pollard et al., 2015), it has already been extensively verified in model in specific studies (Pollard and DeConto, 2020) as well as ice sheet model intercomparisons (Pattyn et al., 2012, 2013; Cornford et al., 2020).

For partial verification of the coupled ice dynamics and thermodynamics, we compare GSM results against a few of the EISMINT (Payne et al., 2000) and HEINO (Calov et al., 2010) SIA model intercomparison results. For the EISMINT experiment G with basal sliding activated everywhere, the GSM simulations preserve the x and y axis symmetry of the forcing (not shown) with most statistics in Table 8 close to the mean value of the intercomparison results in Payne et al. (2000). The one exception is the areal fraction of warm-based ice being just above the minimum value in the intercomparison (note the outlier EISMINT model “U” was removed when calculating means and ranges). This one partial discrepancy is likely attributed to basal sliding

https://doi.org/10.5194/gmd-2024-175
Preprint. Discussion started: 17 January 2025

Geoscientific Model Development
Discussions

Table 7. key GSM fields

Definition	Parameter	units
monthly mean 2 m air temperature	$T_{2m}(x,y)$	^{o}C
ice temperature	Ti(x,y,z)	^{o}C
basal ice temperature with respect to the pressure melting point	$T_{\mathrm{bmp}}(x,y)$	^{o}C
ice velocity	$\mathbf{V} = (u,v)(x,y,z)$	m/yr
basal stress	$\tau_b(x,y)$	Pa
ice thickness	H(x,y)	m
bed elevation relative to present-day sea level	$h_b(x,y)$	m
sea surface geoid	sealev(x,y)	m
bed elevation relative to contemporaneous sea level	$h_{\mathrm{bG}} =$ sealev$-h_b$	m

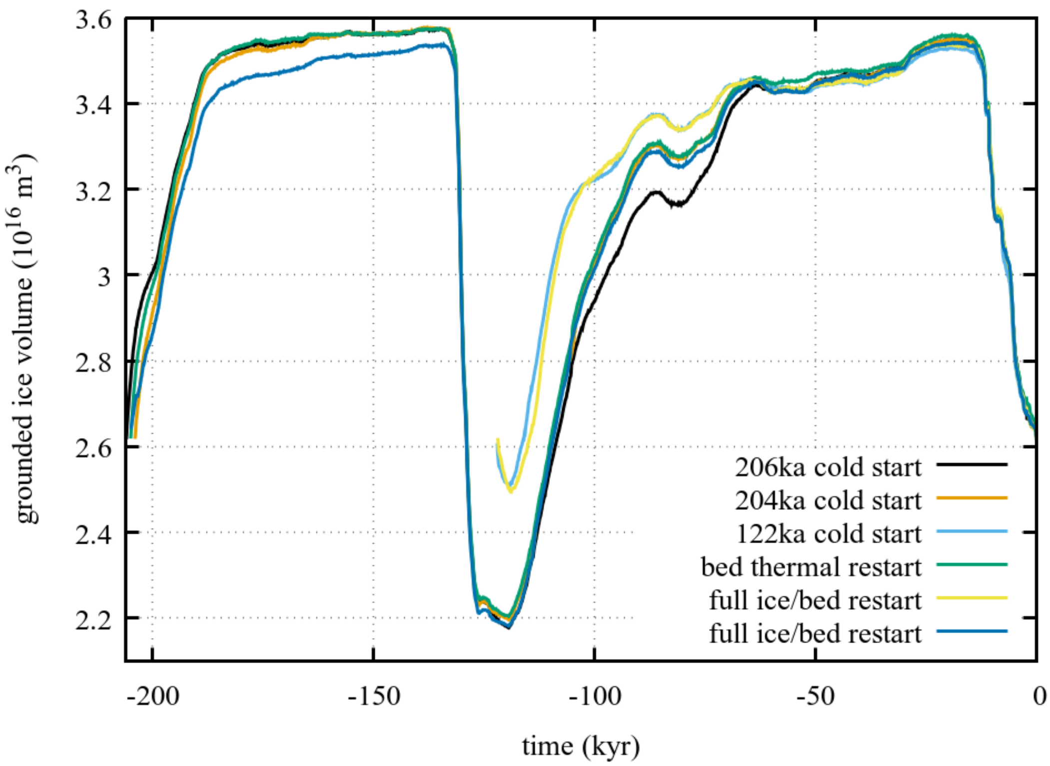

Figure 6. Example AIS ice volume history sensitivity to initialization. As specified in the legend, the last three chronologies use simulations that were initialized from the indicated restart output at the end of full 205 kyr simulations.

https://doi.org/10.5194/gmd-2024-175
Preprint. Discussion started: 17 January 2025

given that the GSM result for the EISMINT A experiment with no basal sliding gives all statistics very close to that of the intercomparison ensemble mean (not shown). Imposition of full SSA ice dynamics everywhere for this configuration induces a slight (3%) decrease in ice volume and even slighter (1.5%) increase in ice area (Table 8).

For EISMINT experiment H with thermal activation of basal sliding, all EISMINT and GSM results are none-steady. GSM maximum and minimum statistics from the last 20 kyr of simulation are within the range of reported EISMINT end of simulation results. However the GSM warm-based fraction is 0.04 below the minimum EISMINT value (only the final time-step values are available from Payne et al., 2000). Similar to the majority of EISMINT models, the GSM experiment H lacks full x and y axis symmetry (not shown).

Table 8. Comparison of GSM results (after 200 kyr simulations) against comparable results for SIA EISMINT G and H experiments (Payne et al., 2000). Listed "EISMINT" results have outlier model U removed. For the GSM SIA experiment H only, the listed minimum and maximum are from the last 20 kyr of simulation (since experiment H never reaches steady state for any model, and EISMINT only provided the last time step results). Both experiments have the same rotationally symmetric climate forcing (and flat bed). The only difference is basal sliding is activated everywhere for experiment G while experiment H uses standard basal temperature dependent sliding activation.

	Volume $10^{15}m^3$	Area $10^{12}m^2$	Warm-based fraction	Divide thickness m	Divide basal temperature ^{o}C
experiment G					
GSM SIA	1.532	1.016	0.261	2223.65	-24.74
GSM SSA	1.487	1.031	0.235	2199.30	-24.64
mean EISMINT	1.520	1.026	0.301	2233.2	-24.65
min EISMINT	1.503	1.016	0.250	2212.6	-25.45
max EISMINT	1.533	1.032	0.351	2228.3	-23.65
experiment H					
GSM SIA min	2.016	1.0094	0.313	3614.8	-17.42
GSM SIA max	2.035	1.0288	0.406	3646.6	-17.41
min EISMINT	1.744	1.020	0.351	3433.1	-19.22
max EISMINT	2.034	1.032	0.622	3645.3	-16.78

To further verify the current coupled ice dynamics/thermodynamics, the standard ISMIP HEINO (Calov et al., 2010) experiment was repeated with various modifications. The climate forcing and boundary conditions for this experiment have full y-axis symmetry but the basal boundary condition is x-axis asymmetric. When run in base hybrid (SIA/SSA) configuration, the simulation has near complete y-axis symmetry (Fig. 7). Symmetry can be further enhanced if basal sliding is activated everywhere (-DwarmBaseEverywhere, Fig. 8). Complete symmetry is obtained when all grid cells are treated as SSA (-DSSAall, not shown).

As for other GSM components, the GSM subgrid hypsometric ice dynamics component verification was carried out in the source reference (Le Morzadec et al., 2015). The surface drainage solver verification again present-day drainage basins is in

https://doi.org/10.5194/gmd-2024-175
Preprint. Discussion started: 17 January 2025

Geoscientific Model Development
Discussions
Open Access
EGU

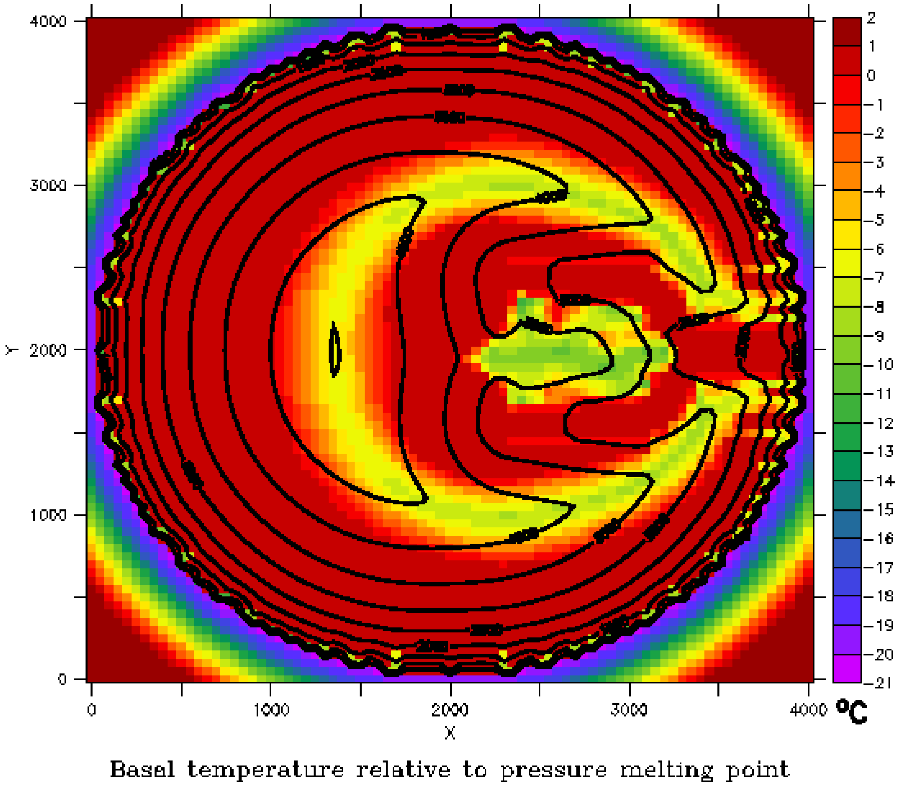

Figure 7. GSM basal temperature relative to the pressure melting point and ice thickness contours for the HEINO experiment with hybrid SIA/SSA.

Tarasov and Peltier (2006). Numerical sensitivity analysis for surge cycling is extensively examined in Hank et al. (2023). For partial verification of the whole ice sheet system, Lecavalier and Tarasov (2024) provides a recent application of the GSM to history matching of the last glacial cycle Antarctic ice sheet that includes comparisons to present-day observations.

Given the nonlinearities in the system, ensemble parameter sensitivities are assessed by automatic relevance determination (Neal, 1996) during the history matching iterations for each paleo ice sheet. For the purposes herein, a simple one at a time parameter sensitivity analysis is provided in the supplement for the Greenland (GRIS), North American (NAIS), and Antarctic (AIS) ice sheets. This has the sole purpose of showing that each ensemble parameter has significant impact for at least one metric component.

https://doi.org/10.5194/gmd-2024-175
Preprint. Discussion started: 17 January 2025

Geoscientific Model Development
Discussions
Open Access

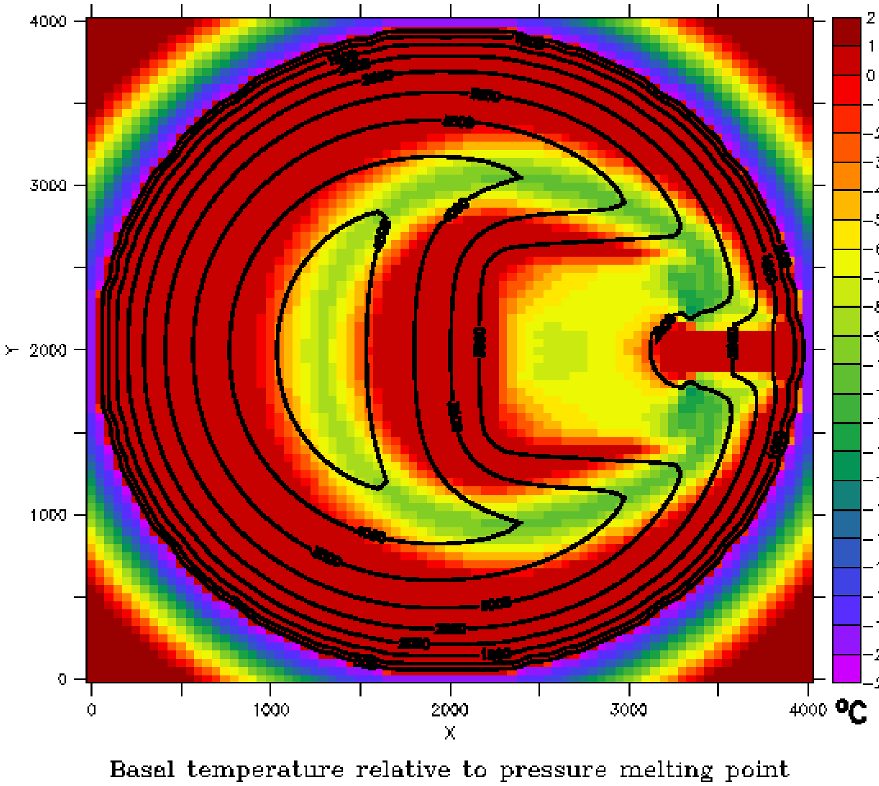

Figure 8. GSM basal temperature relative to the pressure melting point and ice thickness contours for the HEINO experiment with hybrid SIA/SSA and full activation of basal sliding everywhere.

4 Conclusions

The GSM has specific relative strengths and weaknesses compared to other available ice sheet models. The GSM is specifically designed for paleo contexts; where forcing uncertainties necessitate relatively large ensembles of runs along with appropriate methodologies to assess uncertainties and infer parameter vectors consistent with available proxy and observational constraints. As such, it hasn't been parallelized. This can put a strain on available memory resources depending on cluster configuration. For modelling continental-scale ice sheet response to ongoing and projected climate change where high grid resolution (5 km or higher) is much more important than computational cost as well as for coupling to parallelized Earth system models,

https://doi.org/10.5194/gmd-2024-175
Preprint. Discussion started: 17 January 2025

Geoscientific Model Development
Discussions

parallelized ice sheet models such as ISSM (Larour et al., 2012), CISM (Lipscomb et al., 2019), or BISICLES (Cornford et al., 2013) that include the higher order ice dynamical solutions that such high resolutions require would be advised.

The GSM's key strengths for the paleo modelling context are the breadth of relevant incorporated processes, relatively large degrees of freedom in the climate forcing components, and relatively low computational cost (with *e.g.,* an approximately 10 hour wall clock time for a 122 kyr Antarctic simulation at 40 km resolution on a single circa 2016 Intel core including global visco-elastic GIA). The first two features both helps minimize structural uncertainties as well as facilitate simulation comparison against a wide range of paleo proxies. The GSM's computational speed facilitates large ensemble modelling. The GSM's inclusion of process noise injection for internal discrepancy assessment is also to date unique.

A novel feature of the GSM is the PDDsw surface melt scheme that explicitly imposes the physical constraint that shortwave insolation only contributes to surface melt when the surface temperature is at 0^o C. This thereby enables explicit account of changes in spatio-temporal insolation changes on surface melt. It also enables future inclusion of the surface melt impact of surface dust accumulation via changes in surface albedo.

We have demonstrated the importance of three features of the GSM GIA component that are typically ignored for glacial cycle contexts. The geoidal deformation feature will in the future be upgraded to a full pseudo-spectral calculation. The second feature, input of global ice load outside of the ice sheet grid, necessitates some confidence in the global chronology or a move to global ice sheet modelling. The third feature, correcting for present-day isostatic disequilibrium when specifying the initial (Eemian or earlier) topography, is relatively simple to implement for ice sheets that are presently absent. The challenge is that the topographic correction is too sensitive to errors in the simulated present-day ice load for our recursive solution to be viable for regions that are not presently deglaciated.

We have also demonstrated the significant impact of changes in the specification of the basal sliding activation function for Antarctic (Fig. B2) and more so for Greenland (Fig. 1) ice sheet simulations (also cf section 2.5.2). As such, we suggest the appropriate specification of this function (cf Hank et al., 2023) needs more attention within the ice sheet modelling community.

GSM development is ongoing to better ensure that such uncertainties are more confidently bracketed within the range of ensemble parameters and associated process representations with the model. Aside from the over-riding challenge of appropriately representing climate (both atmospheric and oceanic) over glacial cycles, the other least confident components of the GSM (as well as other paleo ice sheet models, if even addressed) are the following. 1) Basal drag as a function of basal roughness, bed geology, and mean sediment thickness (and perhaps class of sediment: clay, till, ...). 2) Subshelf and fjord water temperature, circulation, and salinity and how these fields drive subshelf melt. 3) Lacustrine melt and calving. Aside from climate inputs, the deep geothermal heat flux is a poorly constrained input field for all ice sheets (with potentially significant impact on processes such as Hudson ice stream surge cycling, as shown in Hank and Tarasov, 2024). For regions with present-day ice cover, bed elevation and subgrid bed roughness still have much room for improvement though have already benefited from ongoing efforts (*e.g.,* Morlighem et al., 2017).

The next priority addition to the GSM will be efficient ice age tracing (Rieckh et al., 2024), to enable comparison of simulations against isochronal depth inversions (MacGregor et al., 2015). The other outstanding addition is a fully coupled glaciogenic dust production and deposition on ice (*e.g.,* as in Ganopolski et al., 2010).

https://doi.org/10.5194/gmd-2024-175
Preprint. Discussion started: 17 January 2025

Geoscientific Model Development Discussions

The GSM is currently only available as a tarball with updates available on the lead author's website as per the code availability statement below . Depending on community interest and involvement, a github for the model will likely be setup in the near future.

Code and data availability. A code and input data archive for the GSM is available on Zenodo (https://doi.org/10.5281/zenodo.14599678, Tarasov et al, 2025). Code updates will be available from the first author's website https://www.physics.mun.ca/~lev/software.html .
A tarball of model output for the figures in the text is attached as an asset for this submission.

Appendix A: more technical GSM details

A1 Hybrid SIA/SSA ice dynamics

The heuristic combination of the depth-integrated Shallow Ice Approximation (SIA, vertical shearing) and Shallow Shelf Approximation (SSA, horizontal longitudinal stretching) ice dynamics equations follows (Pollard and DeConto, 2012). The two sets of equations can be linked to each other in three ways:

1. inclusion of shear softening terms when calculating the effective viscosity
2. distinction between the depth-averaged internal-shear and basal velocity in the SSA basal stress term
3. reduction of the SIA driving stress by horizontal shear and longitudinal stress gradient terms from the SSA equations

Each of the three SSA/SIA couplings can be turned on/off individually using compile flags. -DNOSOFTCROSS and -DNOLHSCROSS turn off coupling options 1 and 3, respectively. -DUIACROSS turns on option 2. When using all three coupling options, the SIA-like internal shear equation in x-direction is calculated according to

$$\frac{\partial u_i}{\partial z} = 2A\left[\sigma_{xz}^2 + \sigma_{yz}^2 + \sigma_{xx}^2 + \sigma_{yy}^2 + \sigma_{xy}^2 + \sigma_{xx}\sigma_{yy}\right]^{\frac{n-1}{2}}\sigma_{xz} \tag{A1}$$

where σ_{ij} are the deviatoric stresses. The SSA-like horizontal stretching equation in x-direction is

$$\frac{\partial}{\partial x}\left[\frac{2\mu H}{\bar{A}^{1/n}}\left(2\frac{\partial \bar{u}}{\partial x} + \frac{\partial \bar{v}}{\partial y}\right)\right] + \frac{\partial}{\partial y}\left[\frac{\mu H}{\bar{A}^{1/n}}\left(\frac{\partial \bar{u}}{\partial y} + \frac{\partial \bar{v}}{\partial x}\right)\right] + \tau_{bx} = \rho_i g H \frac{\partial h_s}{\partial x} \tag{A2}$$

where $u_b = \bar{u} - \bar{u}_i$ with bars indicating vertical averages. A similar expression can be found in y-direction and a list of symbols is provided in Table A1. The reduction of the SIA vertical driving stress follows

$$\sigma_{xz} = -\left(\rho_i g H \frac{\partial h_s}{\partial x} - \mathrm{LHS}_x\right)\left(\frac{h_s - z}{H}\right) \tag{A3}$$

where LHS_x is the left hand side in Eq. A2. A similar expression can be found for σ_{yz}. The effective viscosity μ (including the shear softening term) in Eq. A2 is determined by

$$\mu = \frac{1}{2}\left(\dot{\epsilon}^2\right)^{\frac{1-n}{2n}} \tag{A4}$$

https://doi.org/10.5194/gmd-2024-175
Preprint. Discussion started: 17 January 2025

Geoscientific Model Development Discussions

with

$$\dot{\epsilon}^2 \approx \left(\frac{\partial \bar{u}}{\partial x}\right)^2 + \left(\frac{\partial \bar{v}}{\partial y}\right)^2 + \frac{\partial \bar{u}}{\partial x}\frac{\partial \bar{v}}{\partial y} + \frac{1}{4}\left(\frac{\partial \bar{u}}{\partial x}\frac{\partial \bar{v}}{\partial y}\right)^2 + \frac{1}{4}\left(\overline{\frac{\partial u_i}{\partial z}}\right)^2 + \frac{1}{4}\left(\overline{\frac{\partial v_i}{\partial z}}\right)^2 \tag{A5}$$

The above equation can be expressed in terms of σ^2, the purely horizontal components of which are given as

$$\sigma_{xx}^2 + \sigma_{yy}^2 + \sigma_{xy}^2 + \sigma_{xx}\sigma_{yy} = \left(\frac{2\mu}{\bar{A}^{1/n}}\right)^2 \left[\left(\frac{\partial \bar{u}}{\partial x}\right)^2 + \left(\frac{\partial \bar{v}}{\partial y}\right)^2 + \frac{\partial \bar{u}}{\partial x}\frac{\partial \bar{v}}{\partial y} + \frac{1}{4}\left(\frac{\partial \bar{u}}{\partial x} + \frac{\partial \bar{v}}{\partial y}\right)^2\right] \tag{A6}$$

This expression for σ^2 is then used in Eq. A1.

Table A1. Model symbols. Bars indicate vertical averages.

Symbol	Description	Value	Unit
x, y, z	Cartesian coordinates, z increasing upwards	-	m
u, v	horizontal ice velocities	-	$\frac{\mathrm{m}}{\mathrm{yr}}$
u_i, v_i	internal shearing ice velocities	-	$\frac{\mathrm{m}}{\mathrm{yr}}$
u_b, v_b	basal ice velocities	-	$\frac{\mathrm{m}}{\mathrm{yr}}$
H	ice thickness	-	m
h_s	ice surface elevation	-	m
$\bar{A}$	$\int A \frac{dz}{h}$	-	$\frac{1}{\mathrm{yrPa}^3}$
μ	effective viscosity	-	Pa s
m_b	basal sliding exponent	-	-

A2 GSM code structure, time stepping, and recovery from convergence failure

The top-level main GSM routine reads in required inputs, initializes components, and then loops with the asynchronous coupling time step (dlong). Nested flow charts are as follows. Relevant GSM subroutine or variable names are shown within parentheses and relevant source files are enclosed with square brackets.

main program [pGSM.F90]

```
Main time loop with dt=dlong (nc=1,nclim)
   update pCO2, NAHF, and orbital parameters (stepNAHFCO2 and astro)
   run EBM (ebmstep)
   read any time-stepped climate field inputs
   loop over ice sheets  (ice sheet index: ki=1,NICE)
      step icedynGSM (below, all GSM processes aside from GIA and EBM coupling)
   end ice sheets loop
```

https://doi.org/10.5194/gmd-2024-175
Preprint. Discussion started: 17 January 2025

Geoscientific Model Development Discussions
Open Access
EGU

```
  compute sea level field (setsealevG) and new bed topography (pGIA.F90/GIAstep)
end main time loop
```

icedynGSM [pGSMicedynSGhyps.F90]

```
set ice dynamics and thermodynamics timesteps (setIceTimeStep and setThermoTimeStep)
ice dynamics time loop dt=delt (nt=1,ntice)
   compute climate forcing, surface mass balance, subshelf melt,
    and marine and freshwater calving (accumr)
   compute subgrid hypsometric ice flow (fluxhyps.F90/fluxhyps)
   equilibrate thermodynamics for run start (AND nt=1, thermEquil)
   compute basal hydrology (basalHydrology.F90/basalHydrology if
    not using local 0D approximation)
   step ice dynamics (icedyn.F90/Hybridicestep)
   if convergence failure: halve timestep, reset fields, and
    restart ice dynamics time loop
   step thermodynamics (pGSMicetherm.F90/thermo, below)
   step basal sediment processes (sediment)
   further equilibration of thermodynamics with updated ice
    velocities for run start (AND nt=1, thermEquil)
end ice dynamics time loop
compute surface drainage and lake filling (mwpext.F90/compSurfaceDrainage)
output fields and timeseries as required (icedynout, WriteNC)
```

thermodynamics [pGSMicetherm.F90]

```
apply CFL criterion to maximum horizontal velocities to set ice thermodynamic timestep
loop over time
   loop over x,y coordinates
      compute vertical velocity CFL constraints, use 10 times standard
       CFL since the vertical solution is implicit
      use subtime stepping as needed by vertical CFL
      compute matrix elements for discretized thermodynamic equation (compTcoef)
      solve matrix (solvmtrx) while enforcing ice temperature at or below
       pressure melting point
      compute basal melt rate from energy residual from above temperature limiting
      for thin or no ice: use simplified solution algorithm with TTOP
       (temperature above permafrost) or marine corrections
```

https://doi.org/10.5194/gmd-2024-175
Preprint. Discussion started: 17 January 2025

Geoscientific Model Development Discussions

```
    end x,y grid loop
  end time loop
```

To optimize speed, the model computes the ice dynamics time step delt (of value $1/(2^N)$ years, N a whole number) according to CFL constraints based on previous maximum horizontal ice velocities. This is embedded in a larger (default dlong$= 100$ years) time step for GIA, surface drainage, and EBM coupling. If there is complete convergence failure in the ice dynamics, delt is halved, and the calculation is restarted from the beginning of the dlong time interval with recovered ice fields.

Appendix B: GSM numerical sensitivities

Numerical sensitivities are shown for example base parameter vectors with approximately mean parameter values. Mean (10 member) ensemble based sensitivity plots display even less sensitivity to numerical flags (not shown).

For the example GSM Greenland simulation shown in Fig. B1, the only visibly significant ice volume sensitivity of the displayed GSM numerical flags is for the -DTHETANEWA compiler flag enabling the 2D buttressing correction of Pollard and DeConto (2020).

Grounded ice volume sensitivity to GSM numerical flags for an example 122 kyr Antarctic simulation is only significant during the 100 ka to 80 ka interval (Fig. B2). In this case, all compiler flags have a visibly discernible impact, though for some (such as the -DNumDamp compiler flag enabling damping of the iterative solution for the ice thickness) this difference is never more than 2%.

https://doi.org/10.5194/gmd-2024-175
Preprint. Discussion started: 17 January 2025

Geoscientific Model Development
Discussions

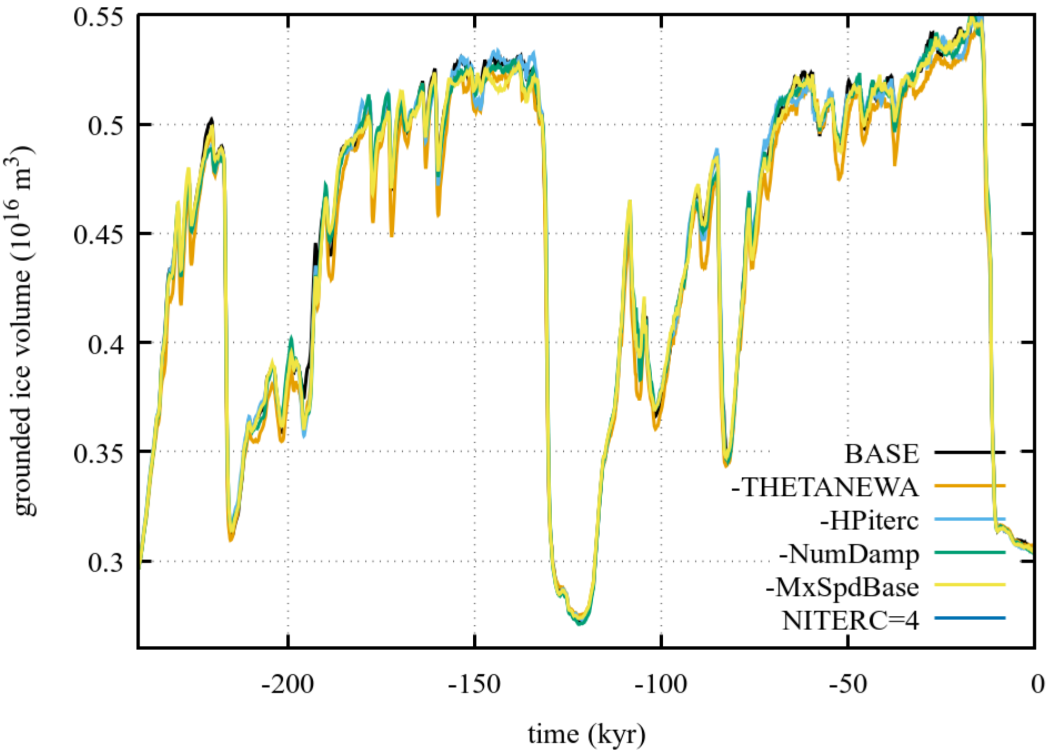

Figure B1. Example GRIS ice volume history sensitivity to numerical compiler flags. The simulations use the default 0.5^o by 0.25^o (longitude, latitude) resolution. Aside from "BASE", simulation key names show the flag that was removed from the recommended default configuration. Removal of MxSpdBase increases the maximum allowed SSA velocity component from 25 km/yr to 30 km/yr. THETANEWA is the revised grounding line flux treatment to address 2D buttressing effects (Pollard and DeConto, 2020). The response to an increase in the maximum number of Picard iterations for the ice thickness solution is keyed by NITERC$= 4$ (default is 3).

https://doi.org/10.5194/gmd-2024-175
Preprint. Discussion started: 17 January 2025

Geoscientific Model Development
Discussions

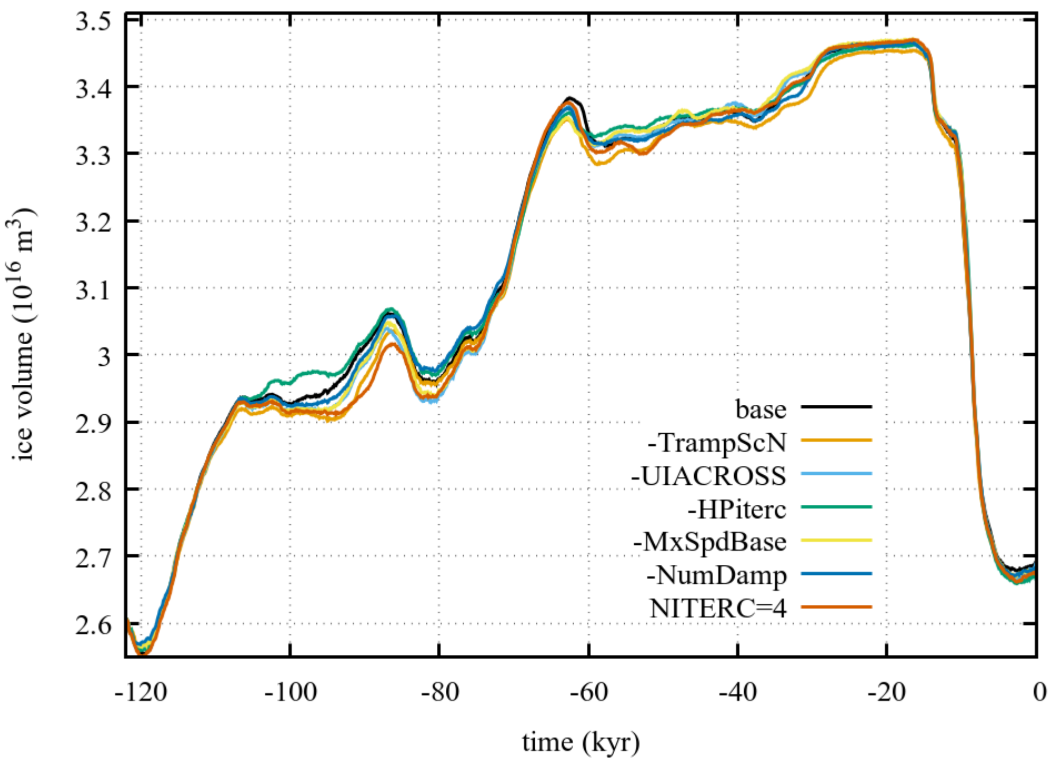

Figure B2. Example AIS ice volume history sensitivity to numerical compiler flags as per previous for GRIS (Fig. B1). TrampScN imposes grid resolution dependence on the basal sliding activation temperature ramp (T_{ramp}) in eq. 13 and eq. 12. The removal of this flag results in T_{ramp} in eq. 12 being nearly twice as large.

https://doi.org/10.5194/gmd-2024-175
Preprint. Discussion started: 17 January 2025

Author contributions. LT wrote this paper with editorial contributions from BL and KH. DP developed the original SIA/SSA hybrid ice dynamics solver as well as the revised grounding line flux treatment to address 2D buttressing effects. BL coupled the SIA/SSA hybrid ice dynamic core, added the Tsai et al. (2015) grounding line flux scheme as well as dual basal drag law capability, and carried out some of the associated validation and verification. BL also acquired and processed the majority of the Antarctic initial and boundary conditions. KH developed and tested the activation function for sub-temperate basal sliding and determined associated numerical sensitivities within the GSM. Unless otherwise specified, LT has developed the remaining components, optimized the SIA/SSA solver, and continues to maintain the GSM.

Competing interests. The authors have no competing interests.

Acknowledgements. GSM development has been partly supported by an NSERC Discovery Grant (number RGPIN-2018-06658) and the Canadian Foundation for Innovation.

https://doi.org/10.5194/gmd-2024-175
Preprint. Discussion started: 17 January 2025

References

Albrecht, T., Winkelmann, R., and Levermann, A.: Glacial-cycle simulations of the Antarctic Ice Sheet with the Parallel Ice Sheet Model (PISM) Part 2: Parameter ensemble analysis, The Cryosphere, 14, 633 656, https://doi.org/10.5194/tc-14-633-2020, 2020.

Andres, H. J. and Tarasov, L.: Towards understanding potential atmospheric contributions to abrupt climate changes: characterizing changes to the North Atlantic eddy-driven jet over the last deglaciation, Climate of the Past, 15, 1621–1646, https://doi.org/10.5194/cp-15-1621-2019, 2019.

Asay-Davis, X. S., Jourdain, N. C., and Nakayama, Y.: Developments in simulating and parameterizing interactions between the Southern Ocean and the Antarctic ice sheet, Current Climate Change Reports, 3, 316–329, 2017.

Bahadory, T. and Tarasov, L.: LCice 1.0 a generalized Ice Sheet System Model coupler for LOVECLIM version 1.3: description, sensitivities, and validation with the Glacial Systems Model (GSM version D2017.aug17), Geoscientific Model Development, 11, 38833 902, https://doi.org/10.5194/gmd-11-3883-2018, 2018.

Bakker, P., Rogozhina, I., Merkel, U., and Prange, M.: Hypersensitivity of glacial summer temperatures in Siberia, CLIMATE OF THE PAST, 16, 371–386, https://doi.org/10.5194/cp-16-371-2020, 2020.

Barker, S., Knorr, G., Edwards, R. L., Parrenin, F., Putnam, A. E., Skinner, L. C., Wolff, E., and Ziegler, M.: 800,000 years of abrupt climate variability, science, 334, 347–351, 2011.

Berends, C. J., Goelzer, H., Reerink, T. J., Stap, L. B., and van de Wal, R. S. W.: Benchmarking the vertically integrated ice-sheet model IMAU-ICE (version 2.0), Geoscientific Model Development, 15, 5667–5688, https://doi.org/10.5194/gmd-15-5667-2022, 2022.

Berger, A. and Loutre, M.: Insolation values for the climate of the last 10 million years, Quaternary Science Reviews, 10, 297–317, https://doi.org/10.1016/0277-3791(91)90033-q, 1991.

Boeira Dias, F., Rintoul, S. R., Richter, O., Galton-Fenzi, B. K., Zika, J. D., Pellichero, V. i., and Uotila, P.: Sensitivity of simulated water mass transformation on the Antarctic shelf to tides, topography and model resolution, Frontiers in Marine Science, 10, https://doi.org/10.3389/fmars.2023.1027704, 2023.

Braconnot, P., Otto-Bliesner, B., Harrison, S., Joussaume, S., Peterschmitt, J.-Y., Abe-Ouchi, A., Crucifix, M., Driesschaert, E., Fichefet, T., Hewitt, C. D., Kageyama, M., Kitoh, A., Lan, A., Loutre, M.-F., Marti, O., Merkel, U., Ramstein, G., Valdes, P., L.Weber, S., Yu, Y., , and Zhao, Y.: Results of PMIP2 coupled simulations of the Mid-Holocene and Last Glacial Maximum - Part 1: Experiments and large-scale features, Climate of the Past, 3, 261–277, 2007.

Braconnot, P., Harrison, S. P., Kageyama, M., Bartlein, P. J., Masson-Delmotte, V., Abe-Ouchi, A., Otto-Bliesner, B., and Zhao, Y.: Evaluation of climate models using palaeoclimatic data, Nature Climate Change, 2, 417–424, 2012.

Bradley, R. S. and England, J. H.: The Younger Dryas and the sea of ancient ice, Quaternary Research, 70, 1–10, 2008.

Braithwaite, R. J.: Positive degree-day factors for ablation on the Greenland ice sheet studied by energy-balance modeling, J. Glaciol., 41, 153–160, 1995.

Budd, W. F. and Smith, I. N.: The growth and retreat of ice sheets in response to orbital radiation changes, in: Sea Level, Ice and Climatic Changes, vol. 131, pp. 369–409, Int. Ass. of Hydrol. Sci., 1981.

Calov, R., Greve, R., Abe-Ouchi, A., Bueler, E., Huybrechts, P., Johnson, J. V., Pattyn, F., Pollard, D., Ritz, C., Saito, F., and Tarasov, L.: Results from the Ice-Sheet Model Intercomparison Project-Heinrich Event INtercOmparison (ISMIP HEINO), J. Glaciol., 56, 371–383, 2010.

https://doi.org/10.5194/gmd-2024-175
Preprint. Discussion started: 17 January 2025

Cornford, S., Martin, D., Graves, D., Ranken, D., Brocq, A. L., Gladstone, R., Payne, A., Ng, E., , and Lipscomb, W. H.: Adaptive mesh, finite volume modeling of marine ice sheets, J. Comput. Phys., 232, 529–549, https://doi.org/10.1016/j.bbr.2011.03.031, 2013.

Cornford, S. L., Seroussi, H., Asay-Davis, X. S., Gudmundsson, G. H., Arthern, R., Borstad, C., Christmann, J., Dias dos Santos, T., Feldmann, J., Goldberg, D., et al.: Results of the third marine ice sheet model intercomparison project (MISMIP+), The Cryosphere Discussions, 2020, 1–26, 2020.

Cuffey, K. and Paterson, W.: The Physics of Glaciers, 4th Edition, Butterworth-Heinemann/Elsevier, Burlington, MA, 2010.

Davies, J. H.: Global map of solid Earth surface heat flow, GEOCHEMISTRY GEOPHYSICS GEOSYSTEMS, 14, 4608–4622, https://doi.org/10.1002/ggge.20271, 2013.

Deblonde, G., Peltier, W. R., and Hyde, W. T.: Simulations of continental ice sheet growth over the last glacial-interglacial cycle: Experiments with a one level seasonal energy balance model including seasonal ice albedo feedback, Glob. and Planet. Change., 98, 37–55, 1992.

Drew, M. and Tarasov, L.: Surging of a Hudson Strait-scale ice stream: subglacial hydrology matters but the process details mostly do not, CRYOSPHERE, 17, 5391–5415, https://doi.org/10.5194/tc-17-5391-2023, 2023.

Drew, M. and Tarasov, L.: North American Pleistocene Glacial Erosion and Thin Pliocene Regolith Thickness Inferred from Data-Constrained Fully Coupled Ice-Climate-Sediment modelling, EGUsphere, 2024, 1–50, https://doi.org/10.5194/egusphere-2024-620, 2024.

Dziewonski, A. M. and Anderson, D. L.: Preliminary reference Earth model, Phys. Earth Planet. Inter., 25, 297–356, 1981.

Fairbanks, R. G.: A 17,000-year glacio-eustatic sea level record: influence of glacial melting rates on the Younger Dryas event and deep-ocean circulation, Nature, 342, 637–641, 1989.

Fausto, R. S., Ahlstrom, A. P., Van As, D., Boggild, C. E., and Johnsen, S. J.: A new present-day temperature parameterization for Greenland, J. Glaciol., 55, 95–105, https://doi.org/10.3189/002214309788608985, 2009.

Favier, L., Jourdain, N. C., Jenkins, A., Merino, N., Durand, G., Gagliardini, O., Gillet-Chaulet, F., and Mathiot, P.: Assessment of sub-shelf melting parameterisations using the ocean–ice-sheet coupled model NEMO (v3.6)–Elmer/Ice (v8.3), Geoscientific Model Development, 12, 2255–2283, 2019.

Forget, G., Campin, J.-M., Heimbach, P., Hill, C. N., Ponte, R. M., and Wunsch, C.: ECCO version 4: an integrated framework for non-linear inverse modeling and global ocean state estimation, Geoscientific Model Development, 8, 3071–3104, https://doi.org/10.5194/gmd-8-3071-2015, 2015.

Fowler, A.: On the rheology of till, in: ANNALS OF GLACIOLOGY, VOL 37, edited by Duval, P., vol. 37 of *Annals of Glaciology-Series*, pp. 55–59, Int Glacier Soc; CNRS; European Space Agc; Reg Rhone Alpes, ISBN 0-946417-32-6, ISSN 0260-3055, https://doi.org/10.3189/172756403781815951, international Symposium on Physical and Mechanical Processes om Ice in Relation to Glacier and Ice-Sheet Modelling, Chamonix, FRANCE, AUG 25-30, 2002, 2003.

Fowler, A. C.: Sub-Temperate Basal Sliding, Journal of Glaciology, 32, 3–5, https://doi.org/10.3189/S0022143000006808, 1986.

Fraedrich, K.: A suite of user-friendly global climate models: Hysteresis experiments, EUROPEAN PHYSICAL JOURNAL PLUS, 127, https://doi.org/10.1140/epjp/i2012-12053-7, 2012.

Fukumori, I., Heimbach, P., Ponte, R. M., and Wunsch, C.: A dynamically consistent, multivariable ocean climatology, Bulletin of the American Meteorological Society, 99, 2107–2128, 2018.

Fulton, R. J.: Surficial materials of Canada, Geological Survey of Canada, Map 1880A, scale 1:5000000, online, 1995.

Gabbi, J., Carenzo, M., Pellicciotti, F., Bauder, A., and Funk, M.: A comparison of empirical and physically based glacier surface melt models for long-term simulations of glacier response, JOURNAL OF GLACIOLOGY, 60, 1140–1154, https://doi.org/10.3189/2014JoG14J011, 2014.

https://doi.org/10.5194/gmd-2024-175
Preprint. Discussion started: 17 January 2025

Geoscientific Model Development Discussions

Ganopolski, A., Calov, R., and Claussen, M.: Simulation of the last glacial cycle with a coupled climate ice-sheet model of intermediate complexity, Clim. of the Past, 6, 229–244, 2010.

Gillet-Chaulet, F., Durand, G., Gagliardini, O., Mosbeux, C., Mouginot, J., Remy, F., and Ritz, C.: Assimilation of surface velocities acquired between 1996 and 2010 to constrain the form of the basal friction law under Pine Island Glacier, GEOPHYSICAL RESEARCH LETTERS, 43, 10 311–10 321, https://doi.org/10.1002/2016GL069937, 2016.

Goelzer, H., Nowicki, S., Edwards, T., Beckley, M., Abe-Ouchi, A., Aschwanden, A., Calov, R., Gagliardini, O., Gillet-Chaulet, F., Golledge, N. R., et al.: Design and results of the ice sheet model initialisation experiments initMIP-Greenland: an ISMIP6 intercomparison, The Cryosphere, 12, 1433–1460, 2018.

Hank, K. and Tarasov, L.: The comparative role of physical system processes in Hudson Strait ice stream cycling: a comprehensive model-based test of Heinrich event hypotheses, EGUsphere, 2024, 1–36, 2024.

Hank, K., Tarasov, L., and Mantelli, E.: Numerical issues in modeling ice sheet instabilities such as binge-purge type cyclic ice stream surging, GMD, 16, 5627–5652, https://doi.org/10.5194/gmd-16-5627-2023, 2023.

Hersbach, H., Bell, B., Berrisford, P., Biavati, G., Horanyi, A., Munoz Sabater, J., Nicolas, J., Peubey, C., Radu, R., Rozum, I., Schepers, D., Simmons, A., Soci, C., Dee, D., and Thepaut, J.-N.: ERA5 monthly averaged data on single levels from 1940 to present, https://doi.org/10.24381/cds.f17050d7, 2023.

Hindmarsh, R. C. and Payne, A. J.: Time-step limits for stable solutions of the ice sheet equation, Ann. Glaciol., 23, 74–85, 1996.

Hock, R.: Temperature index melt modelling in mountain areas, Journal of hydrology, 282, 104–115, 2003.

Hyde, W. T., Crowley, T. J., Kim, K.-Y., and North, G. R.: Comparison of GCM and energy balance model simulations of seasonal temperature changes over the past 18000 years, Journal of Climate, 2, 864–887, 1989.

Irvine-Fynn, T. D. L., Hanna, E., Barrand, N. E., Porter, P. R., Kohler, J., and Hodson, A. J.: Examination of a physically based, high-resolution, distributed Arctic temperature-index melt model, on Midtre Lovenbreen, Svalbard, HYDROLOGICAL PROCESSES, 28, 134–149, https://doi.org/10.1002/hyp.9526, 2014.

Kincaid, D. R., Oppe, T. C., and Joubert, W. D.: An Overview of NSPCG: A Nonsymmetric Preconditioned Conjugate Gradient Package, in: Practical Iterative Methods for Large Scale Computations, edited by Boley, L., Truhlar, D. G., Saad, Y., Wyatt, R. E., and Collins, L. A., pp. 283–293, North-Holland, Amsterdam, 1989.

Krapp, M., Robinson, A., and Ganopolski, A.: SEMIC: an efficient surface energy and mass balance model applied to the Greenland ice sheet, The Cryosphere, 11, 1519–1535, https://doi.org/10.5194/tc-11-1519-2017, 2017.

Kutzbach, J. and Wright Jr, H.: Simulation of the climate of 18,000 years BP: Results for the North American/North Atlantic/European sector and comparison with the geologic record of North America, Quaternary Science Reviews, 4, 147–187, 1985.

Lambeck, K., Rouby, H., Purcell, A., Sun, Y., and Sambridge, M.: Sea level and global ice volumes from the Last Glacial Maximum to the Holocene, Proceedings of the National Academy of Sciences, 111, 15 296–15 303, 2014.

Larour, E., Seroussi, H., Morlighem, M., and Rignot, E.: Continental scale, high order, high spatial resolution, ice sheet modeling using the Ice Sheet System Model (ISSM), Journal of Geophysical Research, 117, F01 022, https://doi.org/10.1029/2011JF002140, 2012.

Laske, G. and Masters, G.: A Global Digital Map of Sediment Thickness, EOS Trans., 78, F483, 1997.

Lazeroms, W. M. J., Jenkins, A., Rienstra, S. W., and van de Wal, R. S. W.: An Analytical Derivation of Ice-Shelf Basal Melt Based on the Dynamics of Meltwater Plumes, JOURNAL OF PHYSICAL OCEANOGRAPHY, 49, 917–939, https://doi.org/10.1175/JPO-D-18-0131.1, 2019.

Le Morzadec, K., Tarasov, L., Morlighem, M., and Seroussi, H.: A new sub-grid surface mass balance and flux model for continental-scale ice sheet modelling: testing and last glacial cycle, Geoscientific Model Development, 8, 3199–3213, https://doi.org/10.5194/gmd-8-3199-2015, 2015.

Lecavalier, B. S. and Tarasov, L.: A history-matching analysis of the Antarctic Ice Sheet since the last interglacial–Part 1: Ice sheet evolution, EGUsphere, 2024, 1–38, https://doi.org/10.5194/egusphere-2024-1291, 2024.

Lecavalier, B. S., Milne, G. A., Simpson, M. J., Wake, L., Huybrechts, P., Tarasov, L., Kjeldsen, K. K., Funder, S., Long, A. J., Woodroffe, S., Dyke, A. S., and Larsen, N. K.: A model of Greenland ice sheet deglaciation constrained by observations of relative sea level and ice extent, Quaternary Science Reviews, 102, 54 – 84, https://doi.org/10.1016/j.quascirev.2014.07.018, 2014.

Lecavalier, B. S., Fisher, D. A., Milne, G. A., Vinther, B. M., Tarasov, L., Huybrechts, P., Lacelle, D., Main, B., Zheng, J., Bourgeois, J., et al.: High Arctic Holocene temperature record from the Agassiz ice cap and Greenland ice sheet evolution, Proceedings of the National Academy of Sciences, 114, 5952–5957, 2017.

Lipscomb, W. H., Price, S. F., Hoffman, M. J., Leguy, G. R., Bennett, A. R., Bradley, S. L., Evans, K. J., Fyke, J. G., Kennedy, J. H., Perego, M., Ranken, D. M., Sacks, W. J., Salinger, A. G., Vargo, L. J., and Worley, P. H.: Description and evaluation of the Community Ice Sheet Model (CISM) v2.1, Geoscientific Model Development, 12, 387–424, https://doi.org/10.5194/gmd-12-387-2019, 2019.

Lisiecki, L. E. and Raymo, M. E.: A Pliocene-Pleistocene stack of 57 globally distributed benthic δ^{18}O records, Paleoceanography, 20, PA1003, https://doi.org/10.1029/2004PA001071, 2005.

Liu, Z., Otto-Bliesner, B. L., He, F., Brady, E. C., Tomas, R., Clark, P. U., Carlson, A. E., Lynch-Stieglitz, J., Curry, W., Brook, E., and et al.: Transient Simulation of Last Deglaciation with a New Mechanism for Bolling-Allerod Warming, Science, 325, 310 314, https://doi.org/10.1126/science.1171041, 2009.

Lofverstrom, M. and Liakka, J.: The influence of atmospheric grid resolution in a climate model-forced ice sheet simulation, The Cryosphere, 12, 1499–1510, https://doi.org/10.5194/tc-12-1499-2018, 2018.

Love, R., Milne, G. A., Tarasov, L., Engelhart, S. E., Hijma, M. P., Latychev, K., Horton, B. P., and Tornqvist, T. E.: The contribution of glacial isostatic adjustment to projections of sea-level change along the Atlantic and Gulf coasts of North America, Earth's Future, 4, 440–464, 2016.

Ma, Y., Gagliardini, O., Ritz, C., Gillet-Chaulet, F., Durand, G., and Montagnat, M.: Enhancement factors for grounded ice and ice shelves inferred from an anisotropic ice-flow model, JOURNAL OF GLACIOLOGY, 56, 805–812, https://doi.org/10.3189/002214310794457209, 2010.

MacGregor, J. A., Fahnestock, M. A., Catania, G. A., Paden, J. D., Prasad Gogineni, S., Young, S. K., Rybarski, S. C., Mabrey, A. N., Wagman, B. M., and Morlighem, M.: Radiostratigraphy and age structure of the Greenland Ice Sheet, Journal of Geophysical Research: Earth Surface, 120, 212 241, https://doi.org/10.1002/2014jf003215, 2015.

Maier, N., Gimbert, F., Gillet-Chaulet, F., and Gilbert, A.: Basal traction mainly dictated by hard-bed physics over grounded regions of Greenland, CRYOSPHERE, 15, 1435–1451, https://doi.org/10.5194/tc-15-1435-2021, 2021.

Maris, M. N. A., de Boer, B., Ligtenberg, S. R. M., Crucifix, M., van de Berg, W. J., and Oerlemans, J.: Modelling the evolution of the Antarctic ice sheet since the last interglacial, CRYOSPHERE, 8, 1347–1360, https://doi.org/10.5194/tc-8-1347-2014, 2014.

Marshall, S. J., Tarasov, L., Clarke, G. K. C., and Peltier, W. R.: Glaciology of Ice Age cycles: Physical processes and modelling challenges, Can. J. Earth Sci., 37, 769–793, 2000.

Melanson, A., Bell, T., and Tarasov, L.: Numerical Modelling of Subglacial Erosion and Sediment Transport and its Application to the North American Ice Sheets over the Last Glacial Cycle, Quat. Sci. Rev., 68, 154–174, 2013.

https://doi.org/10.5194/gmd-2024-175
Preprint. Discussion started: 17 January 2025

Mitrovica, J. and Peltier, W.: A comparison of methods for the inversion of viscoelastic relaxation spectra, Geophysical journal international, 108, 410–414, 1992.

Mitrovica, J. X. and Peltier, W. R.: On Postglacial Geoid Subsidence Over the Equatorial Oceans, J. Geophys. Res., 96, 20,053–20,071, 1991.

Morlighem, M., Williams, C. N., Rignot, E., An, L., Arndt, J. E., Bamber, J. L., Catania, G., Chauché, N., Dowdeswell, J. A., Dorschel, B., et al.: BedMachine v3: Complete bed topography and ocean bathymetry mapping of Greenland from multibeam echo sounding combined with mass conservation, Geophysical research letters, 44, 11–051, 2017.

Mottaghy, D. and Rath, V.: Latent heat effects in subsurface heat transport modelling and their impact on palaeotemperature reconstructions, Geophys. J. Int., 164, 236–245, 2006.

Myhre, G., Highwood, E., Shine, K., and Stordal, F.: New estimates of radiative forcing due to well mixed greenhouse gases, GEOPHYSICAL RESEARCH LETTERS, 25, 2715–2718, https://doi.org/10.1029/98GL01908, 1998.

Neal, R. M.: Bayesian Learning for Neural Networks, vol. 118 of *Lecture Notes in Statistics*, Springer-Verlag, New York, 1996.

Noël, B., van de Berg, W. J., van Wessem, J. M., van Meijgaard, E., van As, D., Lenaerts, J. T. M., Lhermitte, S., Kuipers Munneke, P., Smeets, C. J. P. P., van Ulft, L. H., van de Wal, R. S. W., and van den Broeke, M. R.: Modelling the climate and surface mass balance of polar ice sheets using RACMO2 – Part 1: Greenland (1958–2016), The Cryosphere, 12, 811–831, https://doi.org/10.5194/tc-12-811-2018, 2018.

Osterkamp, T. E.: Freezing and thawing of soils and permafrost containing unfrozen water or brine, Water Resour. Res., 23, 2279–2285, 1987.

Patankar, S. V.: Numerical Heat Transfer and Fluid Flow, Hemisphere, N. Y., 1980.

Pattyn, F., Schoof, C., Perichon, L., Hindmarsh, R. C. A., Bueler, E., de Fleurian, B., Durand, G., Gagliardini, O., Gladstone, R., Goldberg, D., Gudmundsson, G. H., Huybrechts, P., Lee, V., Nick, F. M., Payne, A. J., Pollard, D., Rybak, O., Saito, F., and Vieli, A.: Results of the Marine Ice Sheet Model Intercomparison Project, MISMIP, The Cryosphere, 6, 573–588, https://doi.org/10.5194/tc-6-573-2012, 2012.

Pattyn, F., Perichon, L., Durand, G., Favier, L., Gagliardini, O., Hindmarsh, R. C., Zwinger, T., Albrecht, T., Cornford, S., Docquier, D., et al.: Grounding-line migration in plan-view marine ice-sheet models: results of the ice2sea MISMIP3d intercomparison, Journal of Glaciology, 59, 410–422, 2013.

Payne, A. J., Huybrechts, P., Abe-Ouchi, A., Calov, R., Fastook, J., Greve, R., Marshall, S. J., Marsiat, I., Ritz, C., Tarasov, L., and Thomassen, M.: Results from the EISMINT model intercomparison: the effects of thermomechanical coupling, J. Glaciol., 46, 227–238, 2000.

Peltier, W. R.: The impulse response of a Maxwell Earth, Rev. Geophys., 12, 649–669, 1974.

Peltier, W. R.: Glacial isostatic adjustment II: the inverse problem, Geophys. J. R. Astron. Soc., 46, 669–706, 1976.

Peltier, W. R.: Ice age paleotopography, Science, 265, 195–201, 1994.

Peltier, W. R.: Global glacial isostatic adjustment and the surface of the ice-age Earth: the ICE-5G(VM2) model and GRACE, Annu. Rev. Earth Planet Sci., 32, 111–149, 2004.

Peltier, W. R. and Fairbanks, F. G.: Global Glacial Ice Volume and Last Glacial Maximum Duration from an Extended Barbados Sea Level Record, Quat. Sci. Rev., 25, 3322–3337, 2006.

Pollard, D. and DeConto, R.: Description of a hybrid ice sheet-shelf model, and application to Antarctica, Geoscientific Model Development, 5, 1273–1295, 2012.

Pollard, D. and DeConto, R. M.: Improvements in one-dimensional grounding-line parameterizations in an ice-sheet model with lateral variations (PSUICE3D v2.1), Geoscientific Model Development, 13, 6481–6500, 2020.

Pollard, D., DeConto, R. M., and Alley, R. B.: Potential Antarctic Ice Sheet retreat driven by hydrofracturing and ice cliff failure, Earth and Plan. Sci. Let., 412, 112–121, https://doi.org/10.1016/j.epsl.2014.12.035, 2015.

Quiquet, A., Dumas, C., Ritz, C., Peyaud, V., and Roche, D. M.: The GRISLI ice sheet model (version 2.0): calibration and validation for multi-millennial changes of the Antarctic ice sheet, GEOSCIENTIFIC MODEL DEVELOPMENT, 11, 5003–5025, https://doi.org/10.5194/gmd-11-5003-2018, 2018.

Reese, R., Winkelmann, R., and Gudmundsson, G. H.: Grounding-line flux formula applied as a flux condition in numerical simulations fails for buttressed Antarctic ice streams, The Cryosphere, 12, 3229–3242, 2018.

Reijmer, C. H., van den Broeke, M. R., Fettweis, X., Ettema, J., and Stap, L. B.: Refreezing on the Greenland ice sheet: a comparison of parameterizations, CRYOSPHERE, 6, 743–762, https://doi.org/10.5194/tc-6-743-2012, 2012.

Rieckh, T., Born, A., Robinson, A., Law, R., and Gülle, G.: Design and performance of ELSA v2.0: an isochronal model for ice-sheet layer tracing, Geoscientific Model Development, 17, 6987–7000, https://doi.org/10.5194/gmd-17-6987-2024, 2024.

Rignot, E., Xu, Y., Menemenlis, D., Mouginot, J., Scheuchl, B., Li, X., Morlighem, M., Seroussi, H., van den Broeke, M., Fenty, I., Cai, C., An, L., and de Fleurian, B.: Modeling of ocean-induced ice melt rates of five west Greenland glaciers over the past two decades, GEOPHYSICAL RESEARCH LETTERS, 43, 6374–6382, https://doi.org/10.1002/2016GL068784, 2016.

Robinson, A., Alvarez-Solas, J., Montoya, M., Goelzer, H., Greve, R., and Ritz, C.: Description and validation of the ice-sheet model Yelmo (version 1.0), Geoscientific Model Development, 13, 2805–2823, https://doi.org/10.5194/gmd-13-2805-2020, 2020.

Roe, G. H.: Orographic precipitation, Annu. Rev. Earth Planet. Sci., 33, 645–671, 2005.

Sato, T. and Greve, R.: Sensitivity experiments for the Antarctic ice sheet with varied sub-ice-shelf melting rates, Annals of Glaciology, 53, 221–228, 2012.

Scherrenberg, M. D., Berends, C. J., Stap, L. B., and Van De Wal, R. S.: Modelling feedbacks between the Northern Hemisphere ice sheets and climate during the last glacial cycle, Climate of the Past, 19, 399–418, 2023.

Schoof, C.: Marine ice-sheet dynamics. Part 1. The case of rapid sliding, J. Fluid Mech., 573, 27–55, https://doi.org/10.1017/S0022112006003570, 2007.

Seguinot, J. and Rogozhina, I.: Correspondence: Daily temperature variability predetermined by thermal conditions over ice-sheet surfaces, Journal of Glaciology, 60, 603–605, https://doi.org/10.3189/2014JoG14J036, 2014.

Seroussi, H. and Morlighem, M.: Representation of basal melting at the grounding line in ice flow models, The Cryosphere, 12, 3085–3096, https://doi.org/10.5194/tc-12-3085-2018, 2018.

Seroussi, H., Nowicki, S., Simon, E., Abe-Ouchi, A., Albrecht, T., Brondex, J., Cornford, S., Dumas, C., Gillet-Chaulet, F., Goelzer, H., et al.: initMIP-Antarctica: an ice sheet model initialization experiment of ISMIP6, The Cryosphere, 13, 1441–1471, 2019.

Smith, M. W. and Riseborough, D. W.: Climate and the Limits of Permafrost: A Zonal Analysis, Permafrost Periglac. Process., 13, 1–15, 2002.

Stephens, G., Campbell, G., and Haar, T. V.: Earth radiation budgets, Journal of Geophysical Research: Oceans, 86, 9739–9760, 1981.

Tarasov, L. and Goldstein, M.: Assessing uncertainty in past ice and climate evolution: overview, stepping-stones, and challenges, EGUsphere, 2023, 1–58, https://doi.org/10.5194/egusphere-2022-1410, 2023.

Tarasov, L. and Peltier, W. R.: A high-resolution model of the 100 kyr Ice Age cycle, Ann. Glaciol., 25, 58–65, 1997.

Tarasov, L. and Peltier, W. R.: A geophysically constrained large ensemble analysis of the deglacial history of the North American ice sheet complex, Quat. Sci. Rev., 23, 359–388, 2004.

https://doi.org/10.5194/gmd-2024-175
Preprint. Discussion started: 17 January 2025

Tarasov, L. and Peltier, W. R.: A calibrated deglacial drainage chronology for the North American continent: Evidence of an Arctic trigger for the Younger Dryas, Quat. Sci. Rev., 25, 659–688, 2006.

Tarasov, L. and Peltier, W. R.: The coevolution of continental ice cover and permafrost extent over the last glacial-interglacial cycle in North America, JGR-Earth Surface, 112, doi:10.1029/2006JF000 661, 2007.

Tarasov, L., Dyke, A. S., Neal, R. M., and Peltier, W. R.: A data-calibrated distribution of deglacial chronologies for the North American ice complex from glaciological modeling, Earth and Plan. Sci. Let., 315-316, 30–40, 2012.

Tsai, V. C., Stewart, A. L., and Thompson, A. F.: Marine ice-sheet profiles and stability under Coulomb basal conditions, J. Glaciol., 61, 205–215, https://doi.org/10.3189/2015JoG14J221, 2015.

USGS: USGS EROS Archive - Digital Elevation - HYDRO1K, https://doi.org/10.5066/F77P8WN0, 2004.

van de Berg, W. J., van den Broeke, M., Ettema, J., van Meijgaard, E., and Kaspar, F.: Significant contribution of insolation to Eemian melting of the Greenland ice sheet, NATURE GEOSCIENCE, 4, 679–683, https://doi.org/10.1038/NGEO1245, 2011.

Waelbroeck, C., Labeyrie, L., Michel, E., Duplessy, J., McManus, J., Lambeck, K., Balbon, E., and Labracherie, M.: Sea-level and deep water temperature changes derived from benthic foraminifera isotopic records, Quat. Sci. Rev., 21, 295–305, 2002.

Wake, L. M. and Marshall, S. J.: Assessment of current methods of positive degree-day calculation using in situ observations from glaciated regions, JOURNAL OF GLACIOLOGY, 61, 329–344, https://doi.org/10.3189/2015JoG14J116, 2015.

Whitehouse, P. L., Gomez, N., King, M. A., and Wiens, D. A.: Solid Earth change and the evolution of the Antarctic Ice Sheet, Nature Communications, 10, https://doi.org/10.1038/s41467-018-08068-y, 2019.

Wilkens, N., Behrens, J., Kleiner, T., Rippin, D., Rueckamp, M., and Humbert, A.: Thermal structure and basal sliding parametrisation at Pine Island Glacier - a 3-D full-Stokes model study, CRYOSPHERE, 9, 675–690, https://doi.org/10.5194/tc-9-675-2015, 2015.

Willeit, M., Ganopolski, A., Robinson, A., and Edwards, N. R.: The Earth system model CLIMBER-X v1.0 - Part 1: Climate model description and validation, Geoscientific Model Development, 15, 5905–5948, https://doi.org/10.5194/gmd-15-5905-2022, 2022.

Williams, P. J. and Smith, M. W.: The frozen earth: fundamentals of geocryology, Alden Press, Oxford, 1989.

Winkelmann, R., Martin, M. A., Haseloff, M., Albrecht, T., Bueler, E., Khroulev, C., and Levermann, A.: The Potsdam Parallel Ice Sheet Model (PISM-PIK) - Part 1: Model description, CRYOSPHERE, 5, 715–726, https://doi.org/10.5194/tc-5-715-2011, 2011.